

Magnetic sublattice disorder mediated exchange bias at the interfaces of Ho/Er multilayers in their conical phases

Xiangshang Xiao¹, Kunlong Zhao¹, Yifan Cui¹, Chaofeng Qin¹, Zuoming Wang¹,
Yongxin Yu¹, and Amitesh Paul^{1,2,*}

¹Department of Materials Science and Engineering, and Guangdong Provincial Key Laboratory of Materials and Technologies for Energy Conversion, *Guangdong Technion – Israel Institute of Technology*, 241 Daxue Lu, Shantou, Guangdong 515063, China

²Department of Materials Science and Engineering, *Technion – Israel Institute of Technology*, Haifa 32000, Israel



(Received 23 November 2023; revised 11 March 2024; accepted 6 May 2024; published 4 June 2024)

An increase in spin imbalance induced by magnetic sublattice disorder within rare-earth (RE) metals can in turn increase the exchange bias coupling at the interfaces of RE–RE multilayers below the temperature of conical phases. In this work we have regulated the sublattice disorder by using different monolayers (MLs) of Ho within two highly textured multilayers Ho/Er comprising $ML_{Ho} = 7$ and 29 while keeping $ML_{Er} = 21$. For $ML_{Ho} = 29$, the spin spiral constituting a fraction of the whole stack is expected to decrease the surface area-to-volume ratio and help in the profoundness of the conical phase, thereby contributing to the consequent increase in sublattice disorder. For $ML_{Ho} = 7$, due to its limited extension, the spin spiral is expected to remain truncated and allow a relatively lower disorder. The sample with $ML_{Ho} = 29$ exhibits two temperature-dependent phase transitions of the spin configurations (conical and helical), whereas only a single phase (conical) is identified for the $ML_{Ho} = 7$ sample. Furthermore, a significant shift in temperature for the characteristic peak related to the conical-to-helical phase is observed as compared to an insignificant shift that is related to the helical-to-paramagnetic phase as we decrease the number of Ho MLs from 29 to 7, which eventually reduces the accumulated magnetic repeat distance (10 MLs) by three times. Interestingly, a meager exchange bias field of up to -0.007 kOe ± 0.001 kOe for $ML_{Ho} = 7$ is found to increase by threefold to -0.02 kOe ± 0.005 kOe for $ML_{Ho} = 29$, accounting for the increased sublattice disorder in its conical phase. For $ML_{Ho} = 29$, as we replace 21 MLs of Er with 30 MLs of a ferromagnet (CoFe), we find the usual double hysteresis loops and the coupling strength also increases further to 0.07 kOe ± 0.01 kOe. Thus, the increased exchange bias phenomenon below 20 K in Ho/Er multilayers for the $ML_{Ho} = 29$ sample reflects a higher spin imbalance induced by the magnetic sublattice disorder within Ho.

DOI: [10.1103/PhysRevB.109.224403](https://doi.org/10.1103/PhysRevB.109.224403)

I. INTRODUCTION

Rare earths (REs) are ideal candidates for all-spin-based technology. They possess large orbital momentum, leading to strong spin-orbit coupling or large uniaxial anisotropy along the crystallographic *c* axis and sixfold anisotropy in the basal plane of the crystalline lattice. Several internal interactions, such as exchange, Ruderman-Kittel-Kasuya-Yosida (RKKY), and/or long-range dipolar, influence the information processing via the spin degree of freedom. All these interactions facilitate magnetic modulations, which can coherently propagate across a transition metal (TM) or ferromagnet (FM) over a long range.

Recently, multilayers comprising either a combination of FM/RE materials such as Fe/Tb, Fe/Dy [1–3], or two different RE materials (RE/RE) such as Dy/Tb [4] have been used to investigate topological domain configurations. Exchange bias couplings (≈ 1.0 kOe) in FM/RE or two different RE materials (RE/RE) were found to be exploiting their different (low-high) magnetic anisotropies in realizing such a coupling, as both interfacial layers in the multilayer stacks around the temperature ranges were essentially in their ferromagnetic

phase. However, for RE/RE systems such as Er/Tb [5,6] or Ho/Tb [7], where one of the REs (Er, Ho) is in their conical phase while the other RE (Tb) remains in its FM phase around the same temperature range, a much lower exchange bias (≈ 0.17 –0.75 kOe) can be seen.

For a noncollinear structure within a RE, the pinned spins arise from the small imbalance in the number of spins in each magnetic sublattice due to naturally occurring atomic disorder [8]. The irreversible spins owing to the imbalance are expected to couple with the anisotropic RE helix, the cone, and to the interfacial ferromagnetic spins of the adjacent layer, which in turn would stabilize and thereby cause an exchange bias (H_{eb}) shift. These spins are also accompanied by a reversible component, which explains an increase in the coercive field (H_c). Generally, H_{eb} at an RE/RE interface is expressed as

$$H_{eb} = \frac{\sum n_{ir}^l}{n_{RE} M_{RE}} [-J_{int}], \quad (1)$$

where J_{int} , n_{RE} , and M_{RE} are the internal exchange interaction, number of RE atoms, and magnetic moment of the RE atoms, respectively. $\sum n_{ir}^l$ represents the number of irreversible spins corresponding to each sublattice l in the stack. Within the *n*-vector model in terms of quasiclassical local magnetization vectors [9], the mean-field Hamiltonian for an Ising model ($n = 1$) for simplicity (for a more complex planar model,

*Corresponding author: amitesh.paul@gtiit.edu.cn

TABLE I. Rare-earth anisotropy constants, uniaxial K_u^{RE} , and basal plane K_b^{RE} , where the columns indicate the low- and high-temperature regimes as indicated. Also shown are the temperature ranges of the magnetic phases. In the case of Tb and Dy, in the helical phases (marked in gray) moments are antiferromagnetically modulated along the crystallographic c axis and the low-temperature phase below 221 and 80 K is ferromagnetic (marked in green), respectively. For Er and Ho, the helical phases (marked in cyan) are antiferromagnetically modulated and the low-temperature phase below 20 K is a ferrimagnetic cone phase (marked in lime).

RE	K_u^{RE} ($\times 10^7 \text{ J/m}^3$)	K_u^{RE} ($\times 10^7 \text{ J/m}^3$)	K_b^{RE} ($\times 10^5 \text{ J/m}^3$)	K_b^{RE} ($\times 10^4 \text{ J/m}^3$)	Conical (K)	Helical (K)	Ferromagnetic (K)
[Tb] [10]	5.5 (10 K)	1.7 (200 K)	2.4 (4 K)	2.0 (140 K)	—	229–221	≤ 221
[Dy] [10]	5.0 (22 K)	1.7 (152 K)	7.5 (4 K)	2.0 (120 K)	—	180–80	≤ 80
[Er] [11]	−1.9 (2 K)	—	1.0 (4 K)	—	≤ 20	52–20	—
[Ho] [12]	0.25 (2 K)	0.025 (120 K)	27 (4 K) [13]	—	≤ 20	131–20	—

$n = 2$) can be written as

$$\begin{aligned} \mathcal{H} &= -[J_{\text{inter}} + J_{\text{intra}}] - K_{\text{anisotropy}} \\ &\quad - [J_{\text{imbalance}} + J_{\text{imbalance}}^{\text{intra}}] \\ J_{\text{inter}} &= [J_{\text{RE1-RE2}} S_z^l \langle s_z^l \rangle + J_{\text{RE2-RE1}} S_z^l \langle S_z^l \rangle] \\ J_{\text{intra}} &= [J_{\text{RE1-RE1}} S_z^l \langle S_z^l \rangle + J_{\text{RE2-RE2}} S_z^l \langle s_z^l \rangle] \\ K_{\text{anisotropy}} &= K_{\text{RE1}} S_z^{l2} + K_{\text{RE2}} S_z^{l2} \\ J_{\text{imbalance}}^{\text{intra}} &= J_{\Delta\text{RE1-RE2}} S_z^l \langle s_z^l \rangle + J_{\Delta\text{RE2-RE1}} S_z^l \langle S_z^l \rangle \\ &\quad + J_{\Delta\text{RE2-RE1}} S_z^l \langle S_z^l \rangle + J_{\Delta\text{RE1-RE2}} S_z^l \langle s_z^l \rangle \\ &\quad + J_{\Delta\text{RE1-RE2}} S_z^l \langle s_z^l \rangle + J_{\Delta\text{RE2-RE1}} S_z^l \langle S_z^l \rangle \\ J_{\text{imbalance}}^{\text{intra}} &= J_{\Delta\text{RE1-RE1}} S_z^l \langle S_z^l \rangle + J_{\Delta\text{RE2-RE2}} S_z^l \langle s_z^l \rangle \\ &\quad + J_{\Delta\text{RE1-RE1}} S_z^l \langle S_z^l \rangle + J_{\Delta\text{RE2-RE2}} S_z^l \langle s_z^l \rangle. \end{aligned} \quad (2)$$

Here S_z^l and s_z^l of the l th RE sublattices are the spin operators of the respective sublattice sites of RE1 and RE2. The inter-/intrasublattice contributions are represented by $J_{\text{inter/intra}}$ while the inter-/intraimbalance ($J_{\Delta\text{RE1}}, J_{\Delta\text{RE2}}$) contributions are represented by $J_{\text{imbalance}}^{\text{intra}}$.

The anisotropy constants for REs, which changes with temperature, are tabulated below in Table I. Note that the basal-plane anisotropies (K_b^{RE}) are orders of magnitude lower than those of their uniaxial (K_u^{RE}) counterparts.

The following scenarios can be looked upon following Eq. (2):

(1) RE1 = TM (Fe) and RE2 = Tb, Dy: The intrasublattice exchange terms [$J_{\text{TM1-TM1}} S_z^l \langle S_z^l \rangle + J_{\text{RE2-RE2}} S_z^l \langle s_z^l \rangle$] dominates the intersublattice exchange described by [$J_{\text{TM1-RE2}} S_z^l \langle s_z^l \rangle + J_{\text{RE2-TM1}} S_z^l \langle S_z^l \rangle$], whereas the rare-earth intrasublattice exchange [$J_{\text{RE2-RE2}} S_z^l \langle s_z^l \rangle$] is negligibly small [9]. Note, $K_u^{\text{RE2}} \gg K_u^{\text{Fe}}$ [$K_u^{\text{Fe}} \approx 4.8 \times 10^4 \text{ J/m}^3$ (room temperature, RT)]. Therefore, in Fe/Tb and Fe/Dy systems [1,3], the disappearance of the exchange bias around the temperature range of helical phases in Tb (229–221 K), Dy (180–80 K), is owed to the small number of irreversible spins, i.e., $\Delta\text{TM1} = 0$; $\Delta\text{RE2} \simeq 0$. Below the respective temperatures, as RE2 \rightarrow FM2, the intersublattice exchange terms [$J_{\text{FM1-FM2}} S_z^l \langle s_z^l \rangle + J_{\text{FM2-FM1}} S_z^l \langle S_z^l \rangle$] become non-negligible, which increases H_{eb} , considerably.

(2) RE1 = Dy and RE2 = Tb: Both sublattice exchange terms $J_{\text{inter}} [J_{\text{RE1-RE2}} S_z^l \langle s_z^l \rangle + J_{\text{RE2-RE1}} S_z^l \langle S_z^l \rangle]$ and $J_{\text{intra}} [J_{\text{RE1-RE1}} S_z^l \langle S_z^l \rangle + J_{\text{RE2-RE2}} S_z^l \langle s_z^l \rangle]$ are negligibly small

($\sim 10^{-23} \text{ J}$) [9,14]. Note, K_u^{Dy} and K_u^{Tb} are comparable here. Therefore, in the Dy/Tb system [4], the disappearance of the exchange bias around the temperature range of helical phases in Tb (229–221 K) and Dy (180–80 K) can again be owed to the small number of irreversible spins, i.e., $\Delta\text{RE1} \simeq 0$; $\Delta\text{RE2} \simeq 0$. Below the respective temperatures, as RE1 \rightarrow FM1; RE2 \rightarrow FM2, the intersublattice exchange terms become non-negligible and we found a considerable increase in H_{eb} .

(3) RE1 = Er, Ho and RE2 = Tb. Here also, both sublattice exchange terms J_{inter} and J_{intra} are negligibly small [9] and $K_u^{\text{Ho,Er}}$ and K_u^{Tb} are fairly comparable. Therefore, in Er/Tb [5,6] and Ho/Tb systems [7], the disappearance of the exchange bias around the temperature ranges of helical phases in Er (52–20 K) or Ho (131–20 K) and Tb (229–221 K) is again due to the small number of irreversible spins, i.e., $\Delta\text{RE1} \simeq 0$; $\Delta\text{RE2} \simeq 0$. However, $\Delta\text{RE1} \neq 0$ for Ho or Er in its conical phase below 20 K. The imbalance component ΔRE1 becomes substantially high, and as RE2 \rightarrow FM2, the inter- and intrasublattice exchange terms [$J_{\text{RE1-FM2}} S_z^l \langle s_z^l \rangle + J_{\text{FM2-RE1}} S_z^l \langle S_z^l \rangle$] + [$J_{\text{FM2-FM2}} S_z^l \langle s_z^l \rangle$] and imbalance exchange terms [$J_{\text{FM2-RE1}} S_z^l \langle S_z^l \rangle + J_{\text{RE1-FM2}} S_z^l \langle s_z^l \rangle$] become considerable enough to contribute for a reasonable increase in H_{eb} .

Thus, it would be interesting to explore the situation of exchange bias when RE1 = Ho and RE2 = Er. Below 20 K, one expects $\Delta\text{RE1} \neq 0$ for Ho and $\Delta\text{RE2} \neq 0$ for Er both in their conical phases. A schematic of the basal-plane helix and conical phase transformations of magnetic moments in bulk Ho and Er has been shown in Figs. 1(a)–1(c).

Bulk Ho metal is a basal-plane helical antiferromagnet that exists in between its Curie temperature of about 20 K and the Néel temperature of ~ 131 K [15]. A magnetic field of around 1 T turns the helix into a helifan at around 50 K [16]. The helical structure consists of ferromagnetically ordered moments, which are in the basal planes of the hcp lattice. The moments in each plane are rotated by a certain angle with respect to the neighboring plane; thereby they form a helix along the crystallographic c axis. The magnetic period is temperature dependent with a length of about ten monolayers (MLs) at 40 K, decreasing with increasing temperature to about 7 MLs at the Néel temperature (131 K). Below about 20 K, a cone is the stable phase in zero field and the cone angle is almost independent of the applied field in the basal plane. At low temperatures, the hexagonal anisotropy being large, it forces the magnetic structure to be commensurable with the lattice.

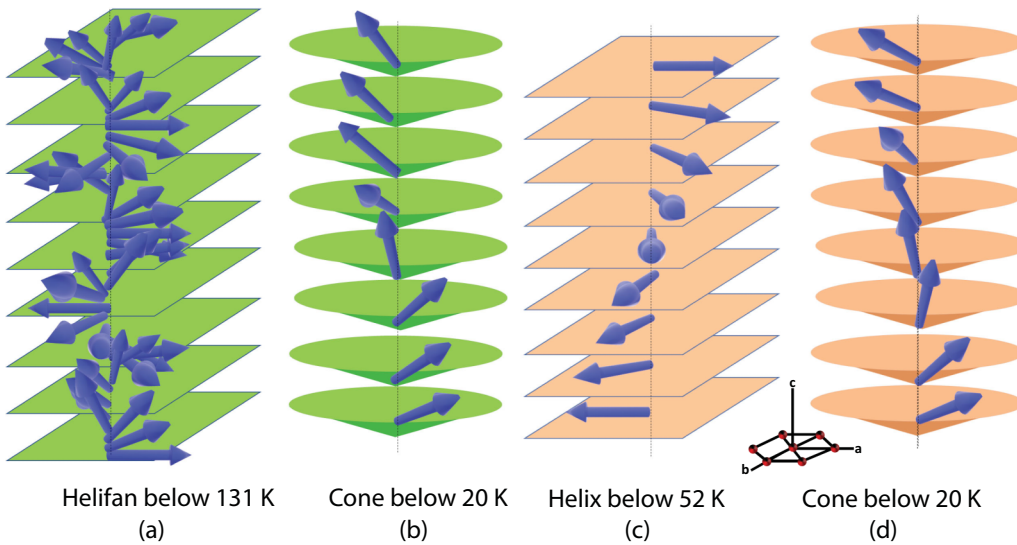


FIG. 1. Sketch of bulk magnetic configurations. Sketch of (a) helifan of Ho in a basal-plane magnetic field, (b) cone phase of Ho, (c) basal-plane helix of Er, and (d) cone phase of Er.

For bulk Er, when the Er spins are cooled below 84 K they are sinusoidally modulated along the c axis, which is referred to as the c axis modulated (CAM) phase. The magnetic wave vector $\tau_c = 2/7$, in units of c^* ($= \frac{2\pi}{c}$), the reciprocal lattice parameter. The magnetic repeat distance is therefore approximately 7 atomic layers. The moments in the hexagonal basal plane order below 52 K with a period similar to the c axis modulation but are confined to the $a - c$ plane in a *cycloidal* structure. As the temperature is reduced, the moments on the individual sites approach their saturation values, resulting in a squaring of the longitudinal wave, which manifests itself into higher odd harmonics [15]. Competing anisotropies result in a complex magnetic structure that develops in a conical c -axis ferromagnetic structure below 20 K ($\tau_c = 5/21$) with a magnetic repeat distance of 7 atomic layers [17–21].

While keeping one of the other RE thicknesses (Er) fixed, we explore two different thicknesses of the other RE (Ho) in Ho/Er multilayers. In the presence of a field, the samples represent commensurable structures, viz., $ML_{Er} = 21$ interfaced with $ML_{Ho} = 7$ and 29. The different thicknesses are expected to differently affect the spin spiral, constituting a fraction of the whole stack, which regulates the effect of surface-area-to-volume ratio. For the $ML_{Ho} = 29$ sample, with a decrease in the surface-area-to-volume ratio, the noncollinear spin configurations in Ho are expected to be affected differently than for the $ML_{Ho} = 7$ sample. The respective phase transition temperatures are found to correspond to the Ho spin spiral rather than Er, which is suspected to remain subdued in both specimens. For the temperature range where one expects conical phases in Ho and Er, we find a meager exchange bias field of -0.007 kOe ± 0.001 kOe for the $ML_{Ho} = 7$ sample. However, where Ho (Er) possesses a spin spiral or helifan (cycloidal) configuration, the exchange bias field is found to be negligibly weak. Interestingly, for the $ML_{Ho} = 29$ sample, the exchange bias field is found to increase up to -0.02 ± 0.01 kOe in the conical phase. As expected, moderate exchange biased fields and double hys-

teresis loops (DHLs) are observed within a RE (Ho)-FM (CoFe) system with $ML_{CoFe} = 30$.

II. SAMPLES AND METHODS

A. Sample preparation

The samples of different compositions were prepared on alumina (0001) substrates by a magnetron sputtering (dc and rf) process.

(1) Sample S1 [Ho₇|Er₂₁]: Nb(100.0 nm)/Y(100.0 nm)/[Ho(2.0 nm)/Er(6.0 nm)]_{N=10}/TaN(2.0 nm).

(2) Sample S2 [Ho₂₉|Er₂₁]: Nb(100.0 nm)/Y(100.0 nm)/[Ho(8.0 nm)/Er(6.0 nm)]_{N=10}/TaN(2.0 nm).

(3) Sample S3 [Ho₂₉|CoFe₃₀]: Nb(100.0 nm)/Y(100.0 nm)/[Ho(8.0 nm)/CoFe(6.0 nm)]_{N=10}/TaN(2.0 nm).

Two reference samples, [Er₇₁₇]: Nb(50.0 nm)/Y(100.0 nm)/Er(200.0 nm) and [Ho₇₂₀]: Nb(100.0 nm)/Y(100.0 nm)/Ho(200.0 nm)/TaN(2.0 nm), were also grown in addition. Here the subscripts in the sample names denote the number of MLs, while the number of bilayers is designated by N . The FM layer CoFe was chosen for its high saturation magnetization and higher magnetic moment ($2.5 \mu_B/\text{atom}$) in bulk as compared to Fe or Co.

For the purpose of growing RE films, we have grown a Nb layer on top of alumina (Al_2O_3) substrate as an effective buffer layer [22]. For the sapphire (1120) plane, the length of the sides equal to 8.241 Å and 12.991 Å, while for the Nb (110) plane, the length of the sides equal to 8.082 Å and 13.336 Å [23,24]. Thus, the sapphire (1120) plane shares a similar basis with the Nb (110) plane. When grown on top of Nb [110], due to the initially strained Nb layer—strained by the alumina substrate—the in-plane axis of hcp Er or Ho [1010] usually suffers an elongation of the c axis lattice parameter. Adding a Y buffer layer between the Nb and Ho layers can cause an opposite effect to the elongation, i.e., a contraction in the c axis lattice parameter [21]. This layer sequence effectively allows an almost unstrained growth of heteroepitaxial RE layers.

Single-crystalline alumina (0001) wafers of dimensions $5 \times 5 \text{ mm}^2$ were used as substrates. Firstly, the wafers were ultrasonically cleaned in isopropyl alcohol and subsequently in acetone and ethanol. Secondly, they were heated to 320°C in vacuum for 20 min before deposition while being mechanically clamped to a sample holder. The targets comprised disks of 2-in. diameter and were cleaned in an Ar atmosphere by presputtering for 1–5 minutes. The thicknesses of the targets were 0.25 in. for Ho (purity 99.9%), 0.25 in. for Er (purity 99.9%), 0.055 in. for Co₈₀Fe₂₀ (purity 99.95%), and 0.125 in. for TaN (purity 99.5%). The TaN target was bonded to a copper backing plate. A compromise between a high-quality crystal structure and a smooth surface for Er and Ho (rms roughness $\approx 0.5 \text{ nm}$) was achieved by depositing at elevated substrate temperatures of 320°C for all layers (including the buffer layers Nb and Y), except for the capping TaN layer. The TaN layer was deposited at RT. The deposition rates were precalibrated (0.08 nm/s for Ho, 0.01 nm/s for Er, and 0.07 nm/s for CoFe). The Ar pressure in the magnetron sputtering chamber was maintained at around $4 \times 10^{-3} \text{ mbar}$ during deposition. The base pressure attained in the chamber was as low as $9.3 \times 10^{-9} \text{ mbar}$.

B. X-ray

A Rigaku SmartLab (9 kW) diffractometer at the GTIIT laboratory was used for x-ray diffraction (XRD) and x-ray reflectivity (XRR), which is equipped with a Cu (Cu $K_{\alpha 1} = 8.04 \text{ keV}$) target.

C. Transmission electron microscopy

We have used a ThermoFisher Talos F200X instrument for specimen preparation to carry out the transmission electron microscopy (TEM) measurements at the Electron Microscopy Center (GTIIT). Using a ThermoScientific Helios 5 DualBeam (SEM/FIB) system, we carried out the sample preparation for the focused ion beam (FIB). We applied typical FIB procedures for the TEM sample preparation with the purpose of reducing the ion-beam-related sample amorphous damage. For the final polishing, low voltages (5 kV and 2 kV) were used, additionally. Using a ThermoFisher Talos F200X TEM operated at 200 kV, high-resolution TEM (HRTEM) observations were performed. A Ceta 16M camera 200 kV and Velox Imaging software were used to record the images. Energy-dispersive x-ray spectroscopy (EDS) experiments were conducted by using a ThermoFisher Talos F200X TEM, which was attached with a Super-X EDS detector. A Velox™ user interface module from ThermoFisher Scientific™ was used in data analysis for the fast Fourier transform (FFT) patterns, and the patterns for different zone axes (ZA) were plotted using the SingleCrystal™ software.

D. Magnetometry

In-plane magnetization measurements were performed conventionally using a superconducting quantum interference device (SQUID) magnetometer from Quantum Design (MPMS3) at the Nanomagnetism and Advanced Scattering Techniques (Nam-AST) laboratory (Paul's Lab) within the GTIIT. The measurements were done following various field-cooling protocols at various temperatures and fields.

III. RESULTS AND DISCUSSIONS

A. X-ray diffraction and reflectivity

Figure 2(a) shows the highly textured XRD profiles for the two reference samples, Er₇₁₇ and Ho₇₂₀. The hex Ho (002) peak can be seen at 31.79° (Ho₇₂₀) and the hex Er (002) peak at 32.01° (Er₇₁₇). Figure 2(b) shows a single peak corresponding to Ho (002) or Er (002) and the other peaks for Y (002) at 30.66° , and Nb (011) at 38.90° for S1–S3. The peaks corresponding to Ho (002) or Er (002) can be seen as a combined peak at 31.74° instead of individual ones, as the structure grows on fairly similar templates. We do not see the polycrystalline CoFe peaks [(110), (200)] from S3, which can be due to the fact that they are mostly overshadowed by the peaks from the capping layer TaN [7].

Figure 3 shows the XRR profile and the corresponding scattering length densities (SLDs) profile for S1 along with its fit as an example. The fit shows the bilayer periodicity from the appearance of the very weak multilayer Bragg peaks and relatively low interface roughnesses for the multilayer structure. The footprint of the x-ray beam (on the order of a few centimeters or tens of millimeters) spans a much larger area than the area under TEM and thereby is of a higher statistical relevance as compared to the TEM images. The footprint is given by a length of $w/\sin\theta$, where w is the beam vertical width ($\sim \mu\text{m}$) and θ is the angle of incidence. One may note that no interdiffused layer is considered in the model structure. The multilayer roughness being similar to the thickness of the thinner layer (here Ho in S1) in the multilayer stack typically indicates a vertically correlated structure [25].

B. Transmission electron microscopy

Figures 4(a), 5(a), and 6(a) show the cross-sectional HRTEM images of S1, S2 and S3. One can readily see the abrupt interfaces between Nb, Y, and the multilayers with clear interface contrast.

FFT patterns of the images concerning the areas containing Nb/Y, Y/[Ho₇|Er₂₁]₁₀; Nb/Y, [Ho₂₉|Er₂₁]₁₀; and Nb/Y, Y/[Ho₂₉|CoFe₃₀]₁₀ are also shown. The respective areas are marked by squares in the HRTEM images within Figs. 4(a), 5(a), and 6(a). The corresponding FFT patterns show the diffraction spots for different ZA: [001] for Ho, [001] for Y, and [111] for Nb in S1 and S2. In S3 the ZA shown are [001] for Ho/CoFe, [001] for Y, and [111] for Nb. Note that the CoFe layers in S3 are rendered polycrystalline, as they have a different crystal structure than the others. The simulations for the FFT patterns are shown along different ZA for Ho, Y, and Nb in S1 and S2, and also for Ho/CoFe, Y and Nb in S3.

Figures 4(b), 5(b), and 6(b) show the high-angle annular dark field scanning TEM (HAADF STEM) images of the interfaces with coherent interface features. HAADF image contrast is mainly related to the differences in atomic number Z as the intensity varies as Z^2 . Elemental identifications of Nb, Y, Ho, and Er across the stack are shown in the corresponding EDS maps of S1 and S2. Similar elemental identifications of Nb, Y, Ho, and Co across the stack are shown in the corresponding EDS maps of S3. The HAADF STEM images show an out-of-plane grain size that approximately matches the film thickness, extended up to $\sim 145\text{--}195 \text{ nm}$, perpendicular to the

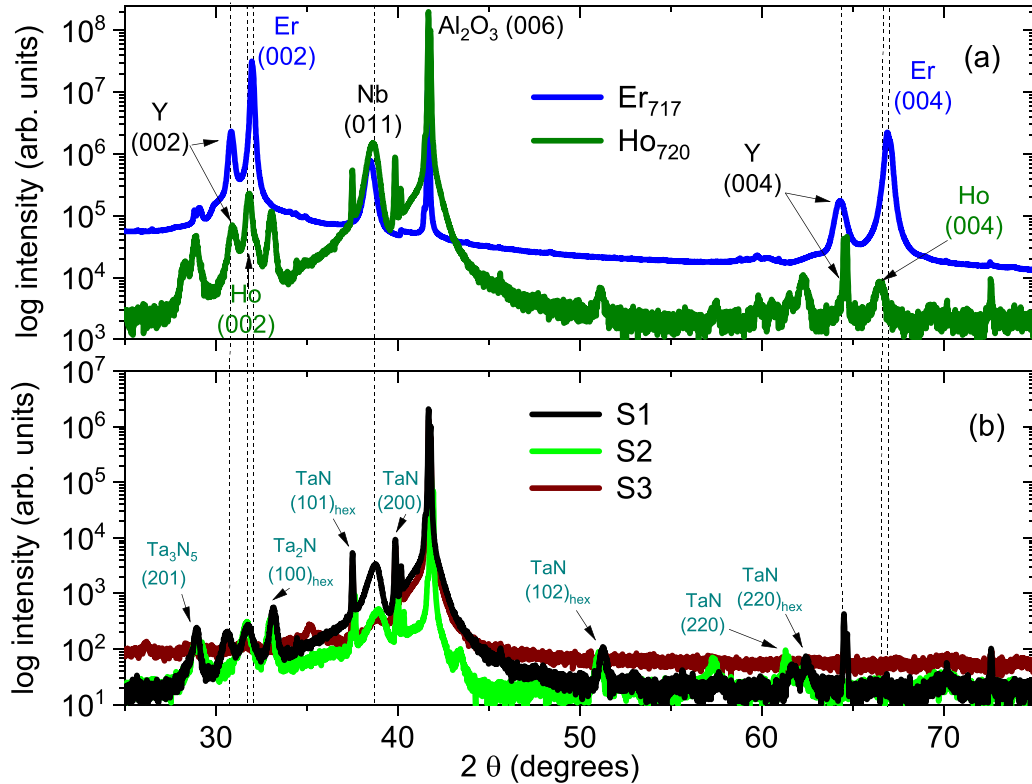


FIG. 2. XRD for S1–S3. (a) X-ray diffraction of the thin films indicating the main structural peaks from films, buffers, and substrate for the two reference samples, Er_{717} and Ho_{720} . (b) The XRD peaks of highly textured multilayers S1, S2, and S3 are similar to that of single layers of Er, Ho and are indicated by the dashed lines. The peaks corresponding to the various polycrystalline phases of TaN-based compounds are also indicated.

film plane. Grain sizes \geq a few tens of nanometers increase the temperature stability in the layered structure where the interfaces restrict interdiffusion.

The color contrasts between Ho and Er layers in their respective EDS elemental maps cannot be strictly considered as the true representatives of the layer quality, leading to wrong interpretation of their interface disorder. Note that the TEM

method is limited to a very small observation area, and EDS is still unable to account for many factors that can greatly affect the accuracy of an analysis such as surface or interface roughness. The unclear bilayer periodicity is primarily due to the lack of x-ray characteristic energy contrast between Ho ($L_{\alpha} = 6.72 \text{ keV}; Z = 67$), Er ($L_{\alpha} = 6.94 \text{ keV}; Z = 68$) and Co ($K_{\alpha} = 6.92 \text{ keV}; Z = 27$). The typical energy resolution for EDS is kept at around 100–150 eV for a similar energy range. For our experiment we calibrate EDS at the Mn $K\alpha$ edge with a resolution of 134 eV. Thus, the color code contrasts cannot be strictly considered representative of their interface disorder, as they are only a rough guidance of Ho and Er in the stack. The contrast gets more diluted the greater the scan area. Moreover, due to the increased interdiffusion related to the loss of interfacial structural coherency on account of polycrystalline CoFe in S3, the boundaries appear more blurred in the EDS map of S3 than in S1 or S2.

In order to clarify the repeated bilayer structure, we present in Fig. 7(a) a more detailed EDS maps at a smaller length scale for S1, S2, and S3 with different color codes of the atomic fraction percentages for Ho and Er in S1 and S2 and for Co and Fe in S3. The corresponding line profiles are also shown in Fig. 7(b). The periodic structures are clearly evident from the vertical line profiles, at least for S1 and S2. The periodicity is blurred in S3. The bilayer periodicity appears more distinguishable in S2 than in S1 due to the lower Ho thickness in S1. The horizontal line profiles show their low interface roughnesses ($\sigma_{\text{rms}} = 0.08 \pm 0.02 \text{ at } \%$).

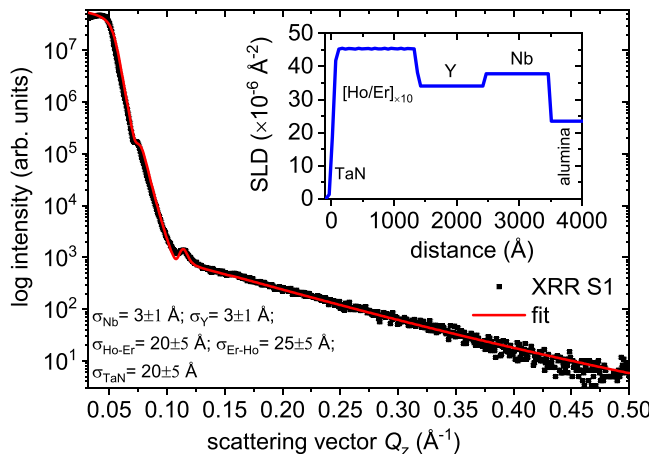


FIG. 3. XRR for S1. XRR profile vs scattering vector Q_z for the multilayer S1 and its fit without employing a footprint correction. Inset shows the corresponding SLD profile of the layer structure. The roughnesses of the multilayer indicate a typical vertically correlated structure.

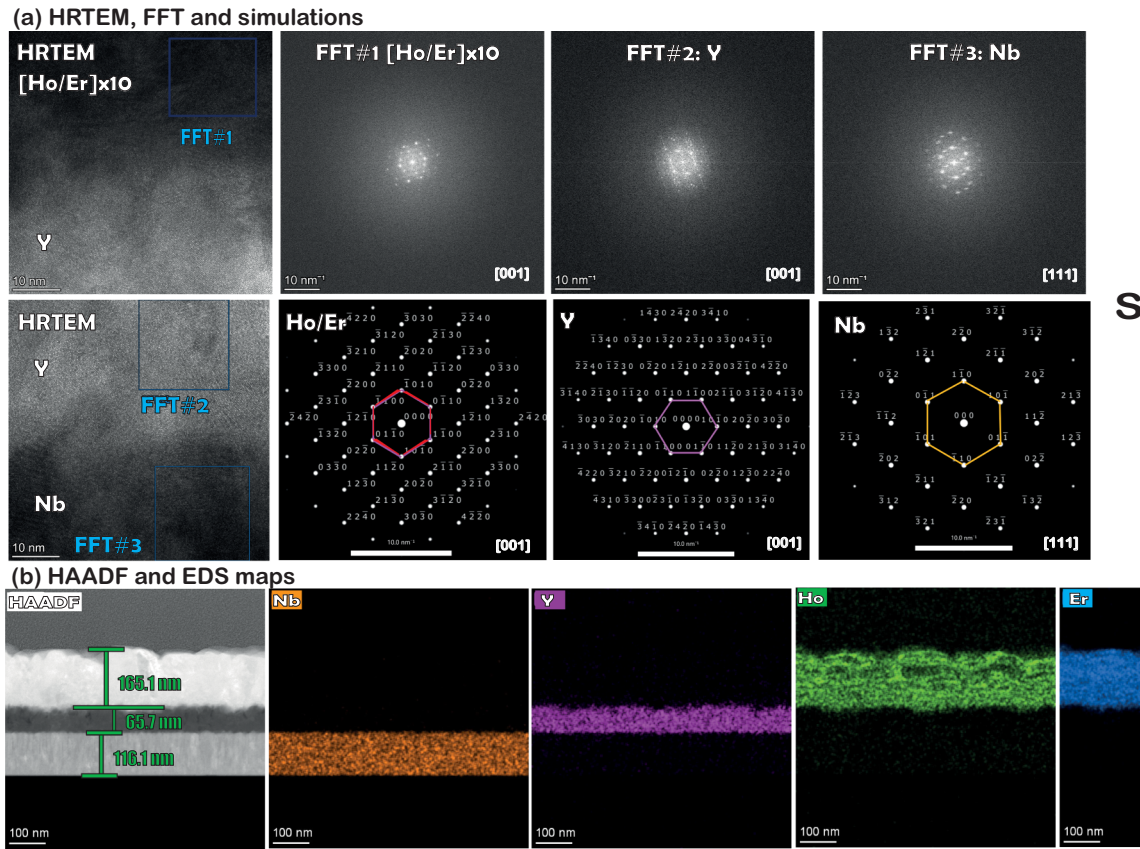


FIG. 4. HRTEM, FFT, simulations, and EDS for S1. (a) Cross-sectional HRTEM images of specimen S1, showing the layer sequence on alumina substrate. The corresponding FFT patterns of the area marked by the squares in the HRTEM images containing Nb/Y and Y/[Ho(2.0 nm)/Er(6.0 nm)] $_{xN=10}$ interfaces are also shown. Simulations for the FFT patterns for different zone axes: [001] for Ho, [001] for Y, and [111] for Nb are shown corresponding to the FFT patterns. The respective hexagonal spots (marked in pink), the hexagonal spots (marked in magenta), and the hexagonal spots (marked in yellow) corresponding to the multilayer, Y, and Nb are also depicted. (b) The HAADF STEM image along with the EDS maps of the elements Nb, Y, Ho, and Er in the layer stack showing the interfaces.

C. Magnetization measurements

a. Field hysteresis loops

In-plane magnetic field hysteresis loops were measured at different temperatures for S1, S2, and S3 at various temperatures after field-cooling in the presence of +70 kOe (7000 mT). The hysteresis loops for S1, S2, and S3 are shown in Figs. 8(a)–8(l), Figs. 9(a)–9(l), and Figs. 10(a)–10(l). The samples saturate at a field of ≈ 40 kOe. The two branches of the hysteresis loops, decreasing and increasing, give the respective remanent magnetization ($m_r = [m_r^+ - m_r^-]/2$), coercivity ($H_c = [H_c^+ - H_c^-]/2$), and exchange bias ($H_{eb} = [H_c^+ + H_c^-]/2$).

The zoomed-in hysteresis loops at 30 K, 50 K and 2 K, 170 K (S1) are shown in Figs. 8(m) and 8(n), at 30 K, 50 K and 2 K, 170 K (S2) in Figs. 9(m) and 9(n), and at 30 K, and 2 K, 170 K (S3) in Figs. 10(m) and 10(n) within the field ranges of limited values.

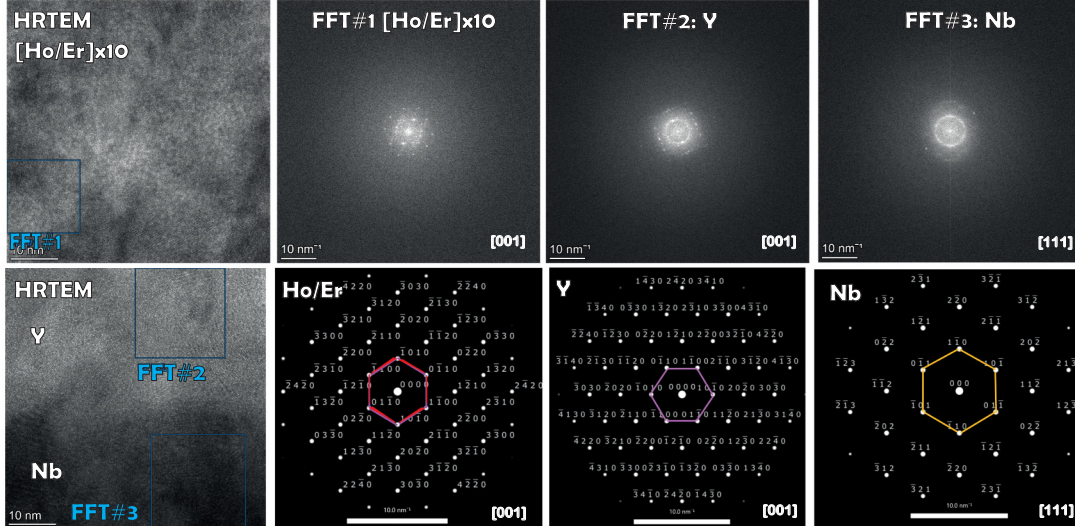
Superposition of two hysteresis loops (primary and secondary) have been reported earlier for Fe/Tb [1] and also in Fe/Dy [3] systems, which is known as a “double hysteresis loop” (DHL). We designate H_{eb}^1 and H_{eb}^2 for primary and secondary loop shifts, respectively. Oppositely biased subsystems with equal magnitudes of exchange bias acting on the DHLs

make them symmetric. DHLs are seen between at 50 K in S1 [Fig. 8(m)], below 50 K in S2 [Fig. 9(m)], and below 170 K in S3 [Figs. 9(m) and 9(n)]. Please note that the DHLs in S3 [Fig. 10(n)] are the most prominent ones. This is because the CoFe layer remains FM below RT, which leads to stronger coupling.

In Figs. 11(a), 12(a), and 13(a) we plot the monotonic decrease of m_r and H_c , and the variations of H_{eb} with increasing T for S1, S2, and S3. Both m_r and H_c go to zero at $T = 50$ K for both S1 and S2. The temperature where $H_{eb} \rightarrow 0$ signifies an apparent blocking or freezing temperature of the Ho/Er system, magnetically coupled. For S3, H_c goes to zero at 250 K but m_r never goes to zero even at RT. Whereas S1 and S2 indicate an apparent superparamagnetic or super-spin-glass (SPM/SSG), for any blocking or freezing type of behavior in the system, S3 does not indicate a SPM/SSG type of behavior.

For S1, at temperatures below 130 K where the Ho or Er layer is supposed to remain in a conical-to-helical or cycloidal (marked in lime-cyan) and cycloidal-to-sinusoidal phase for Er (marked in cyan-blue), we find a maximum $H_{eb}^1 = -0.007 \pm 0.005$ kOe at 30 K from the primary loop [Fig. 11(b)]. The H_{eb}^1 value is seen to be fluctuating even

(a) HRTEM, FFT and simulations



S2

(b) HAADF and EDS maps

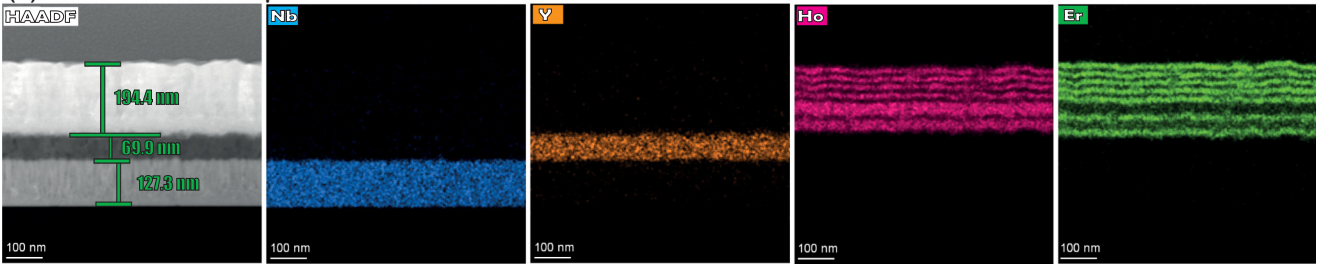


FIG. 5. HRTEM, FFT, simulations, and EDS for S2. (a) Cross-sectional HRTEM images of specimen S1, showing the layer sequence on alumina substrate. The corresponding FFT patterns of the area marked by the squares in the HRTEM images containing Nb/Y and Y/[Ho(8.0 nm)/Er(6.0 nm)] $\times N=10$ interfaces are also shown. Simulations for the FFT patterns for different zone axes: [001] for Ho, [001] for Y, and [111] for Nb are shown corresponding to the FFT patterns. The respective hexagonal spots (marked in pink), the hexagonal spots (marked in magenta), and the hexagonal spots (marked in yellow) corresponding to the multilayer, Y, and Nb are also depicted. (b) The HAADF STEM image along with the EDS maps of the elements Nb, Y, Ho, and Er in the layer stack showing the interfaces.

changing its sign with increasing temperature. We see indications of DHL at 50 K, but no H_{eb}^2 could be found from the loop shifts.

For S2, we find a maximum $H_{\text{eb}}^1 = -0.02 \pm 0.005$ kOe at 2 K [Fig. 12(b)], and its value is seen to be fluctuating often changing its sign with increasing temperature before dying out at 300 K [Fig. 12(c)]. Below 20 K, both Ho and Er are expected to be in their conical phase, and around the temperature range between 20 and 52 K or between 20 and 131 K, a helical or helifan spin configuration is expected, above which negligible exchange bias fields can be seen, signifying a very weak coupling between Ho and Er. We attribute the exchange bias to the spin imbalance in each magnetic conical sublattice disorder [8]. When an interface monolayer reconstructs into a sufficiently rigid canted moments configuration, the coupling phenomenon as a function of temperature results in uncertainty during each field-cooling process contributing to the spin imbalance [26]. Significant H_{eb}^2 can be seen for S2 from 2 K onwards, reaching a maximum $H_{\text{eb}}^2 = \pm 11.0 \pm 1$ kOe at 50 K.

One may note that for an increase in the number of MLs from $ML_{\text{Ho}} = 7$ to $ML_{\text{Ho}} = 29$, we find a threefold increase in H_{eb}^1 . Usually, for such an increase in FM (Tb) MLs in the case of Ho/Tb [7] or Er/Tb [6] multilayers within a similar

temperature range, earlier we found a decrease in H_{eb}^1 . This increase in the bias field in the Ho/Er multilayer therefore indicates an increase in the spin imbalance due to increased sublattice disorder for an extended spin spiral within $ML_{\text{Ho}} = 29$. Interestingly, the magnetic repeat distance of 10 MLs below 40 K also increases approximately by threefold while going from $ML_{\text{Ho}} = 7$ to $ML_{\text{Ho}} = 29$.

For S3, a maximum $H_{\text{eb}}^1 = +0.07 \pm 0.005$ kOe at 20 K [Fig. 13(b)] and oscillating with increase in temperature is seen as its value continuously decreases in magnitude without any change in sign. A maximum $H_{\text{eb}}^2 = \pm 9.0 \pm 1$ kOe at 20 K is seen [Fig. 13(c)]. The similar maximum values of H_{eb}^1 , H_{eb}^2 in the present sample [Ho₂₉/CoFe₃₀] and in a previous sample [Ho₂₉/CoFe₁₀] ($H_{\text{eb}}^1 = -0.02 \pm 0.005$ kOe at 2 K; $H_{\text{eb}}^2 = \pm 11.0 \pm 1$ kOe at 30 K) [7] can be attributed more to the contributions of sublattice exchange terms rather than the influence of thickness of the FM (CoFe) layer.

The H_{eb}^1 values are found fluctuating in S1 and S2, going from positive to negative (or negative to positive) values. Such fluctuations stem from the respective antiferromagnetic (or ferromagnetic) coupling at the Ho/Er interfaces during the field-cooling processes. Positive or negative exchange bias

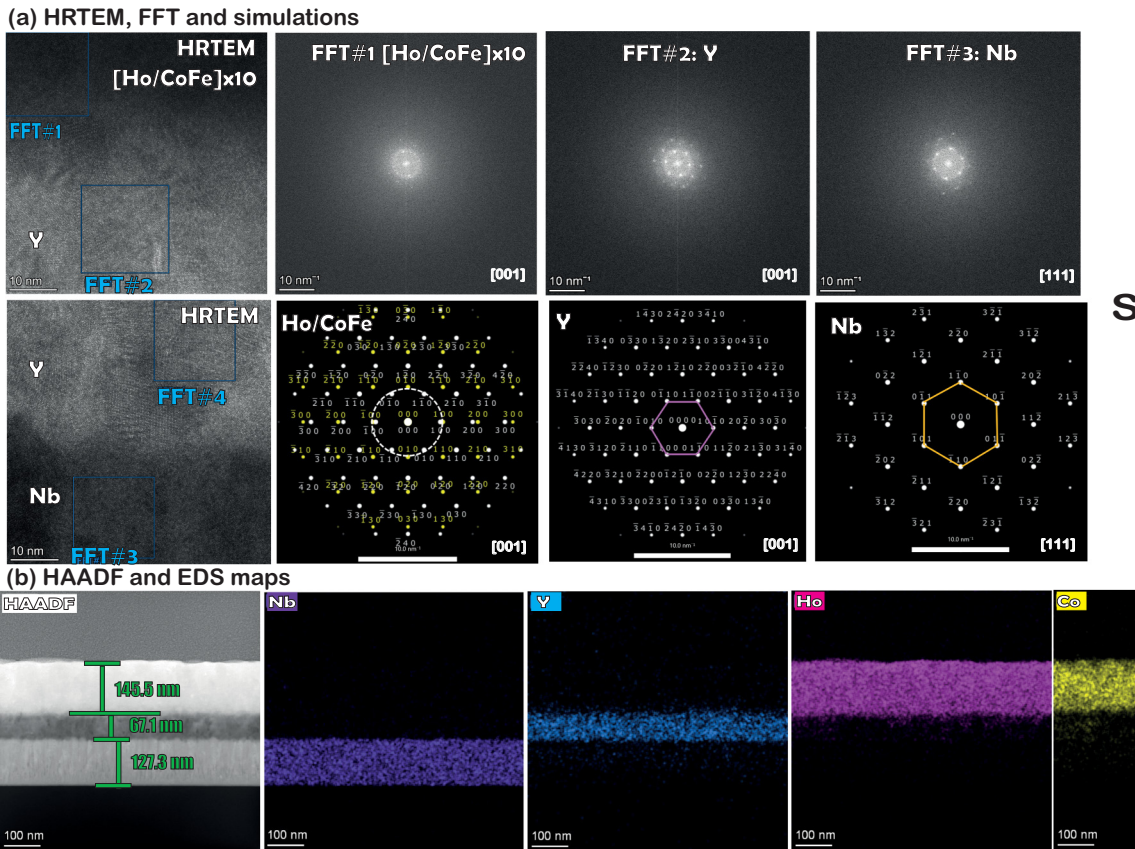


FIG. 6. HRTEM, FFT, simulations, and EDS for S3. (a) Cross-sectional HRTEM images of specimen S3, showing the layer sequence on alumina substrate. The corresponding FFT patterns of the area marked by the squares in the HRTEM images containing Nb/Y and Y/[Ho(8.0 nm)/CoFe(6.0 nm)] $\times N=10$ interfaces are also shown. Simulations for the FFT patterns for different zone axes: [001] for Ho, [001] for Y, and [111] for Nb are shown corresponding to the FFT patterns. The respective hexagonal and rectangular spots (marked in white circle), the hexagonal spots (marked in magenta), and the hexagonal spots (marked in yellow) corresponding to the multilayer, Y, and Nb are also depicted. (b) The HAADF STEM image along with the EDS maps of the elements Nb, Y, Ho, and Co in the layer stack showing the interfaces.

may occur when an antiferromagnetic interface monolayer reconstructs into a sufficiently rigid canted moment configuration [26], which is a highly plausible scenario for the conical phase within Ho or Er. For S3 also, we find the H_{eb}^1 values to oscillate but remain positive at all temperatures. The oscillations in S3 are owed to the conical-helical phases in Ho. Overall, the fluctuating coupling as a function of temperature in S1–S3 results from the uncertainty in the small imbalance for the number of spins in each magnetic conical and helical sublattice disorder, which may creep in during each field-cooling protocol [8].

Both H_c as well as m_r indicate relaxation and magnetic irreversibility for $T < T_F$, typical for supermagnetic blocked or frozen spin clusters [27]. Here the blocking or freezing temperature is given by T_F . One can apply an external field to reduce the energy barrier against the anisotropy appropriate for SPM-SSG relaxation. At a certain magnetic field (coercive field) the magnetization can effectively disappear, which is given by the equation

$$H_c = 2 \frac{K_u}{m_s} \left[1 - \left(\frac{T}{T_F} \right)^{\frac{1}{2}} \right]. \quad (3)$$

The equation holds for an ensemble of noninteracting clusters of spins (SPM), where m_s is the saturation magnetization and K_u is the anisotropy constant [28].

The H_c versus $T^{1/2}$ plot in Fig. 11(c) shows a linear behavior for S1. The respective temperature where H_c cuts the $T^{1/2}$ axis is given by the corresponding blocking or freezing temperatures $T_{F1}(0) = 55$ K in S1. For S2, the corresponding values for $T_{F1}(0) = 40$ K and $T_{F2}(0) = 76$ K are shown in the inset of Fig. 12(a) [5,6]. On the one hand, a nonlinear behavior generally indicates spin clustering of SSG type in case both m_r and H_c go to zero. A linear behavior, on the other hand, can be a signature of spin clustering of SPM-SSG type. One may note that at the temperature range between 20 and 52 K for Er (20 and 131 K for Ho) one expects a helical or cycloidal (helifan) spin configuration within Er (Ho). Thus, the linear regions in the H_c versus $T^{1/2}$ plots in S1 and S2 indicate an apparent nanoclustering or a regular FM behavior. Note that the $T^{1/2}$ plots alone cannot discern the SPM or SSG type of behaviors.

As expected, a nonlinear behavior can be seen for S3 from the H_c versus $T^{1/2}$ plots in the inset of Fig. 13(a). Such a nonlinear behavior, which is obviously due to the presence of CoFe, indicates a regular FM type of behavior.

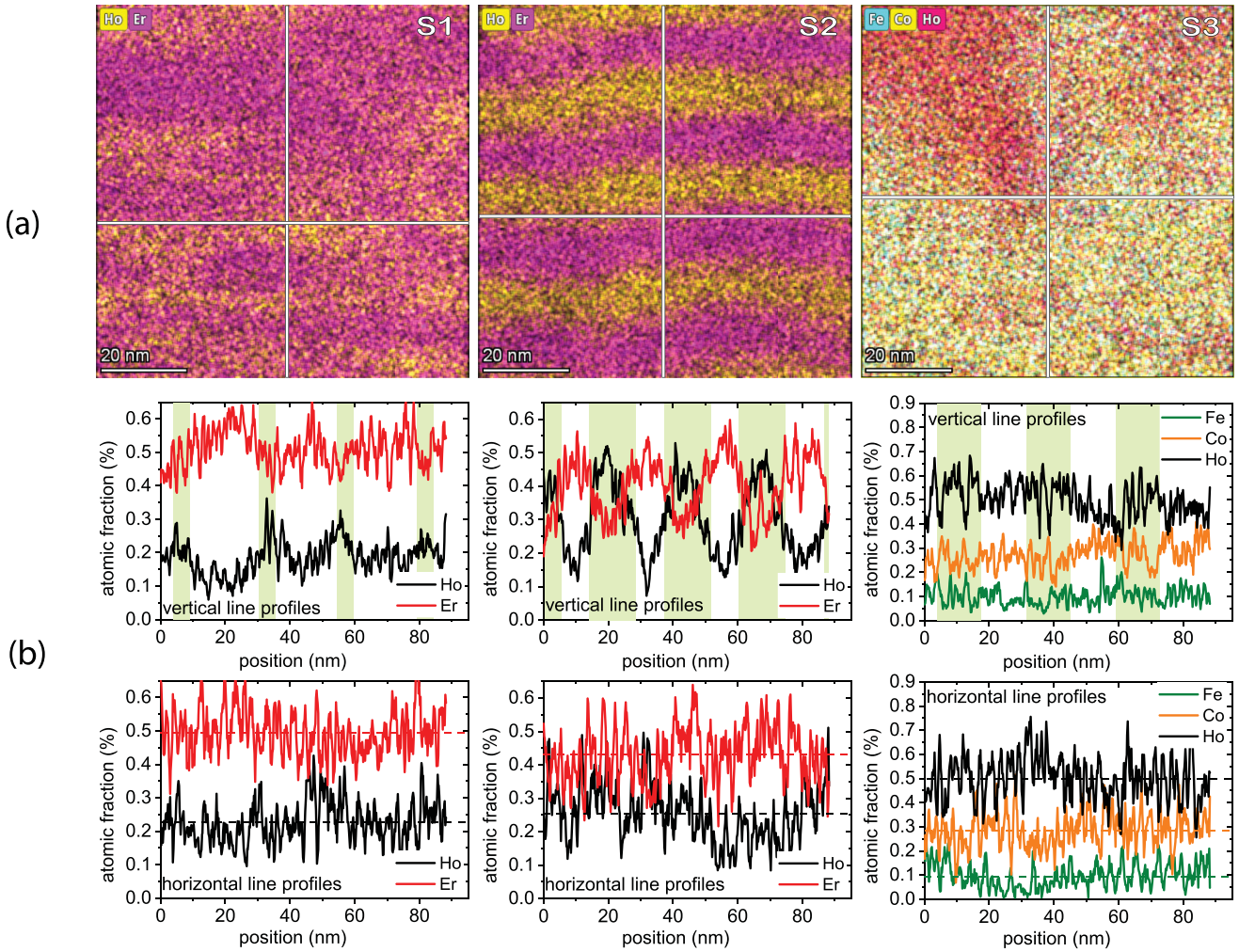


FIG. 7. EDS for S1, S2, and S3. (a) EDS maps of the elements Ho, Er and Co, Fe in the layer stack showing the bilayer periodicity and interface roughness in S1, S2, and S3. (b) Vertical and horizontal line profiles of atomic fraction percentages from the images showing the bilayer periodicity and interface roughness. The shaded regions in lime mark the presence of Ho in the stack for the vertical profiles. The dotted lines mark the mean positions of the atomic fractions at the respective layer interfaces for the horizontal profiles.

For S1 the linear behavior is seen between a temperature range 0–55 K (r_{S1}^1), where the curve intercepts the x axis, whereas for S2 they are between 0 and 33 K (r_{S2}^1), where the curve deviates from linearity. This temperature range is related to the conical-to-helical phase within Ho or Er. Additionally, another temperature regime is seen between 33 and 76 K (r_{S2}^2) for S2, which can be related either to the helical-to-paramagnetic phase within Ho or to the helical-to-paramagnetic phase within Er. Therefore, there exist two different nanoclustering behaviors within two different temperature regimes (r^1 and r^2) for S2. Note that there exists no r_{S1}^2 , which indicates an absence of the signature of second phase change in Er ($ML_{Er} = 21$). Thus it can be argued that the signature of phase change from helical-to-paramagnetic in S2 is due to the influence of the increased number of Ho MLs on Er MLs. Alternatively, the appearance of r_{S2}^2 can solely be related to the phase change within Ho, and we can consider that the signature of Er phase change remains subdued in S2, as both S1 and S2 possess the same number of Er MLs ($ML_{Er} = 21$).

Furthermore, as we go from $ML_{Ho} = 7$ to $ML_{Ho} = 29$, the first range is $\Delta r_{S1}^1 = 55$ K and $\Delta r_{S2}^1 = 33$ K. Thus, the first temperature limit changes from 55 to 33 K or is shifted to lower temperature by 22 K for S2. This indicates the profoundness of the conical phase in Ho as it approaches closer to the bulk value. The second range $\Delta r_{S2}^2 = 43$ K, as the limit changes from 33 to 76 K. The shifts in $r_{S1,S2}^1$ and appearance of r_{S2}^2 can therefore be related to the higher Ho layer thickness in S2, effectively influencing the temperature regimes of the two magnetic phases within Ho. For the $ML_{Ho} = 29$ sample, a decrease in the surface-area-to-volume ratio is expected as compared to the $ML_{Ho} = 7$ sample. This change in ratio would in turn affect the noncollinear spin configurations differently or contribute to the profoundness of the helix in Ho.

b. Field-cooled and zero-field-cooled measurements

Using field-dependent magnetization (M) measurements as a function of temperature (T), characterizations of the magnetic properties were done upon standard field-cooled (FC)

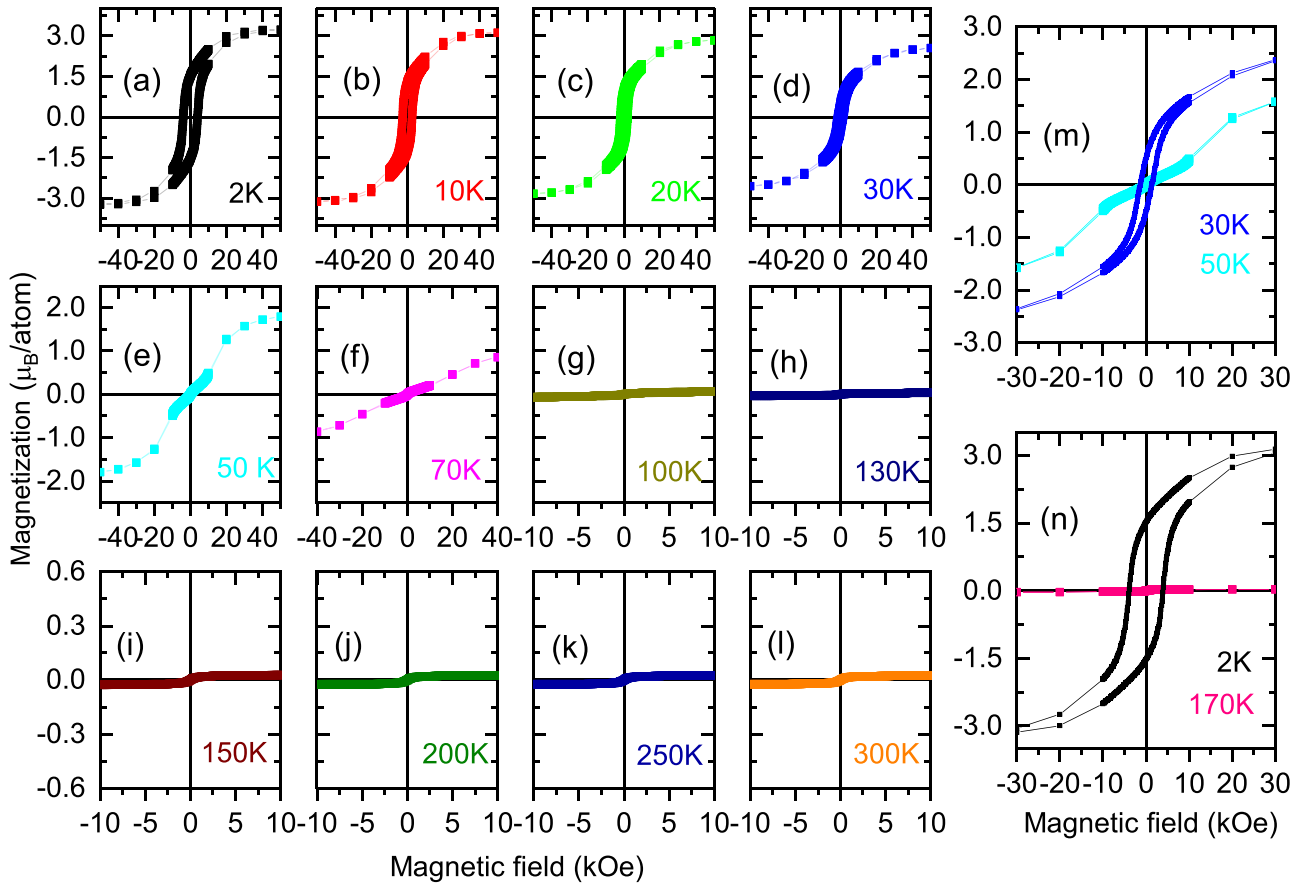


FIG. 8. Hysteresis loops for S1. (a)–(l) Hysteresis loops at various temperatures showing different shifts of the loops with temperature after field-cooling. (m), (n) Zoomed-in plots of the loop shifts rendering $H_{eb}^{-/+}$ values at 30 K, 50 K (DHL), and 2 K, 170 K.

and zero-field-cooled (ZFC) protocols. We applied different magnetic fields $\mathbf{H}_a = 10$ Oe (1 mT) to 1000 Oe (100 mT) during measurements after cooling to 2 K in the presence of $\mathbf{H}_a = 70$ kOe/7000 mT (FC) for S1, S2, and S3. The same protocol was used when the samples were cooled to 2 K in the presence of zero magnetic field (ZFC). The magnetization [$M(T)$] curves are shown in Figs. 14(a), 14(b), 15(a), 15(b), and Fig. 16(a), 16(b) in various applied fields for S1, S2, and S3, respectively.

For S1 [Fig. 14(b)] we can see two peaks at $T_{F1} = 33 \pm 2$ K and a smaller peak $T_{F2} = 82 \pm 4$ K, which are around the temperature region of the conical-to-helical phase transition of Ho or Er and sinusoidal-to-paramagnetic phase of Er. Note that the basal-plane component of Ho(Er) orders from a paramagnetic(sinusoidal) phase into a helical(cycloidal) structure below 131 K(52 K). For $ML_{Ho} = 7$, the Ho spin spiral being poorly constituted, we do not find any peak around the temperature associated with the helical phase of the Ho layers in S1 [7]. For S2 [Fig. 15(b)] one can see a peak $T_{F1} = 20 \pm 2$ K, which is around the temperature region of the conical-to-helical phase of Ho, and a smaller peak at $T_{F2} = 89 \pm 4$ K, which is around the temperature region of the sinusoidal-to-paramagnetic phase of Er. Here also, for $ML_{Ho} = 29$ no peak can be related to Ho around the temperature of the helical phase of Ho (20–131 K). This disappearance can be due to the similar number of MLs in Er and Ho affecting the spin spirals of each other.

Thus, following the magnetization versus temperature curves for $ML_{Ho} = 7$ and 29, a shift or lowering by 13 K (33–20 K) is observed in the characteristic peak (T_{F1}) around the low-temperature regime, and an insignificant increase by 7 K (82–89 K) for the characteristic peak (T_{F2}) around the high-temperature regime is observed. One may note that following the H_c versus $T^{1/2}$ plots for $ML_{Ho} = 7$ and 21 [insets of Figs. 11(a) and 12(a)], a definitive shift or decrease in $T_{F1}(0)$ by 15 K (55–40 K) while going from S1 to S2 and appearance of $T_{F2}(0)$ in S2 at 76 K are observed. These shifts indicate that the state of the helical phase formation in Ho is affecting the conical-to-helical and helical-to-paramagnetic (or sinusoidal-to-paramagnetic) phase fractions within Ho (or Er) in Ho/Er multilayers.

In comparison, a shift in $T_{F1}(0)$ (increased by 16 K), T_{F1} (increased by 9 K), and T_{F2} (increased by 50–100 K) was observed earlier in Er/Tb multilayers due to a change in the Tb MLs from $ML_{Tb} = 5$ –21 [6]. Note that when Tb is in the FM phase, it affects the Er spin spiral in a way that extends the temperature regimes of conical and helical phases. However, in the present case, when both REs are in their noncollinear phases, the increase in Ho MLs helps in the profoundness of the phases and thereby lowering the temperature regime of the conical phase, driving it closer to the bulk values.

Furthermore, $T_{F1,F2}$ are not influenced by the applied fields for S1 and S2. For $ML_{Ho} = 29$, the turn angle is accumulated

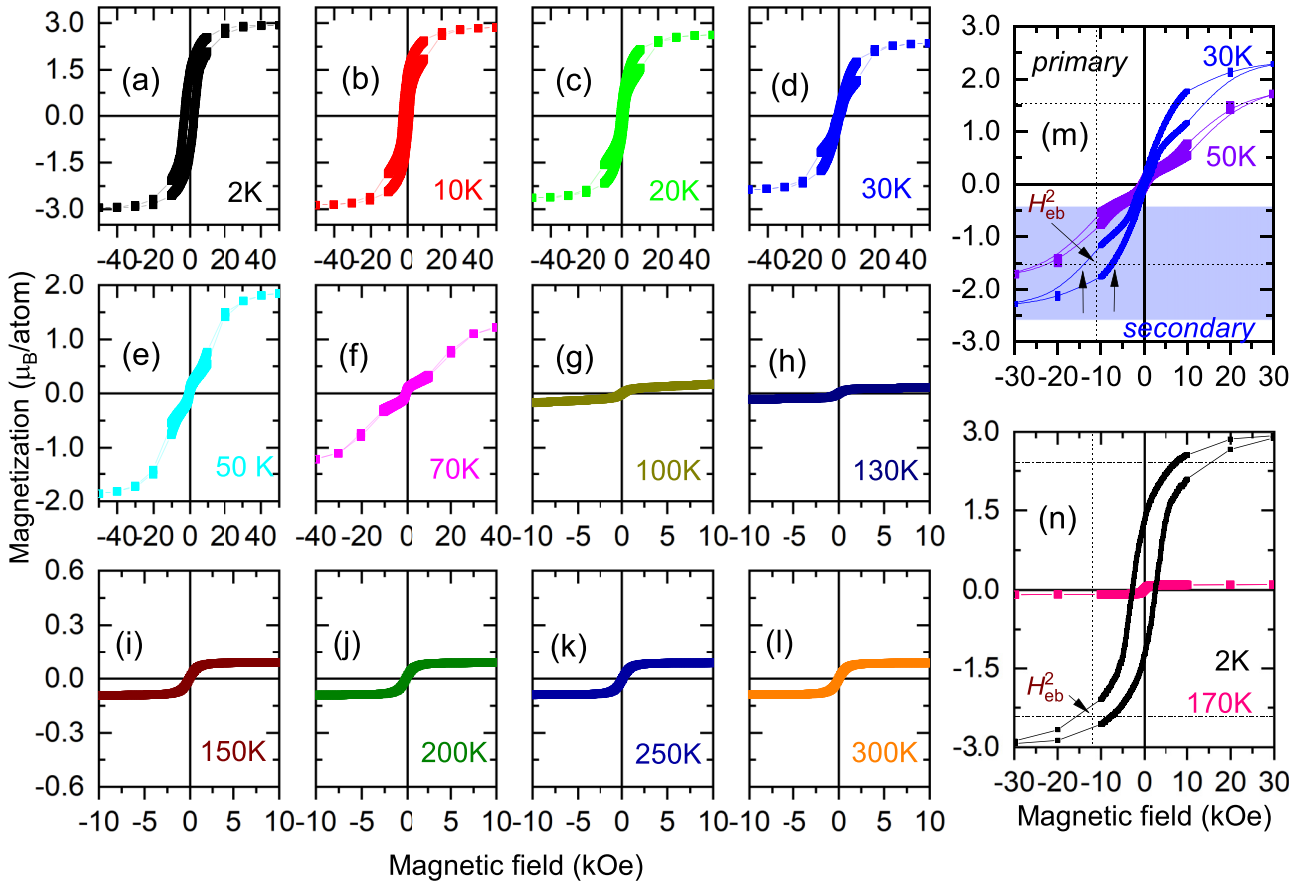


FIG. 9. Hysteresis loops for S2. (a)–(l) Hysteresis loops at various temperatures showing different shifts of the loops with temperature after field-cooling. (m), (n) Zoomed-in plots of the loop shifts rendering $H_{eb}^{-/+}$ values at 30 K (DHL), 50 K (DHL) and 2 K, 170 K. The black arrows indicate the two coercive fields of DHL at 30 K, while the shaded region in blue indicates the region of the secondary loop at the bottom half of the loop. The H_{eb}^2 values are indicated by arrows in the bottom half of the loops at 30 and 2 K.

across different atomic layers of Ho, depending upon the temperature regimes (≈ 30 or 3×10 MLs below 40 K) / ≈ 28 or 4×7 MLs below 131 K). Therefore, the fraction of the spin spiral in Ho is limited for $ML_{Ho} = 7$. Note that a convergence of the FC-ZFC curves can be ascertained for S1 and S2. However, the field dependence of the irreversibility temperature T_{irr} indicates no field dependence. The divergence of ZFC and FC, therefore, suggests some kind of magnetic frustration. Such frustration can arise either due to the coexisting ferromagnetic (FM) and antiferromagnetic (AF) phases or due to noninteracting superparamagnetic particles. No thermomagnetic irreversibility is expected for a purely ferromagnetic transition, whereas for a weak ferromagnet or a frustrated system with mixed FM-AF phases, irreversibility may be expected. Thus, both S1 and S2 show typical FM behaviors [5].

For S3 the FC-ZFC curves shown in Figs. 16(a) and 16(b) possess typical ferromagnetic behavior. From the zoomed-in plots in Fig. 16(b), we find $T_{FO} = 9$ K. The presence of T_{FO} is a typical signature of the spin-flop characteristic reported earlier [6]. We also find a third peak, $T_{F3} = 275\text{--}200$ K, which decreases gradually with the application of the field. The negative magnetization below 200 K is due to the competing interaction of coexisting FM-AF phases originating from the FM (CoFe) layer. In this regard, note that topologically protected nontrivial structures are hard to destroy by

a magnetic field when applied perpendicular to the domain orientation, which essentially gives their topological stability. For S3, however, due to their larger values of $ML_{CoFe} = 30$, the plausibility of spin-frustrated interfaces increases. Thus, T_{F3} in S3 is found to be lowered with the increasing applied field as shown in Fig. 17(a). The peak shift (T_{F3}) signifies that the frozen or blocked state is gradually suppressed by the field. With an increase in the magnetic field, as the crystal-field anisotropy starts to decrease, it also decreases the thermal energy required to cross the height of energy barriers between the two easy-axis orientations.

The irreversibility temperature T_{irr} can be interpreted as an indicator of the existence of a blocking or freezing temperature distribution associated with a particle size distribution. The T_{irr} values are seen to be shifting towards low temperatures with increasing \mathbf{H}_a , and they can follow the Almeida-Thouless (AT) line, signifying an SSG-like behavior [29,30]. The expression for the AT line,

$$\mathbf{H}_a/\Delta J \propto \left(1 - \frac{T_{irr}(\mathbf{H}_a)}{T_{irr}(0)}\right)^{\frac{3}{2}}, \quad (4)$$

includes $T_{irr}(0)$, which is the zero-field freezing temperature, while ΔJ represents the width of the distribution of exchange interactions. Usually, such a curve when fitted to the AT line

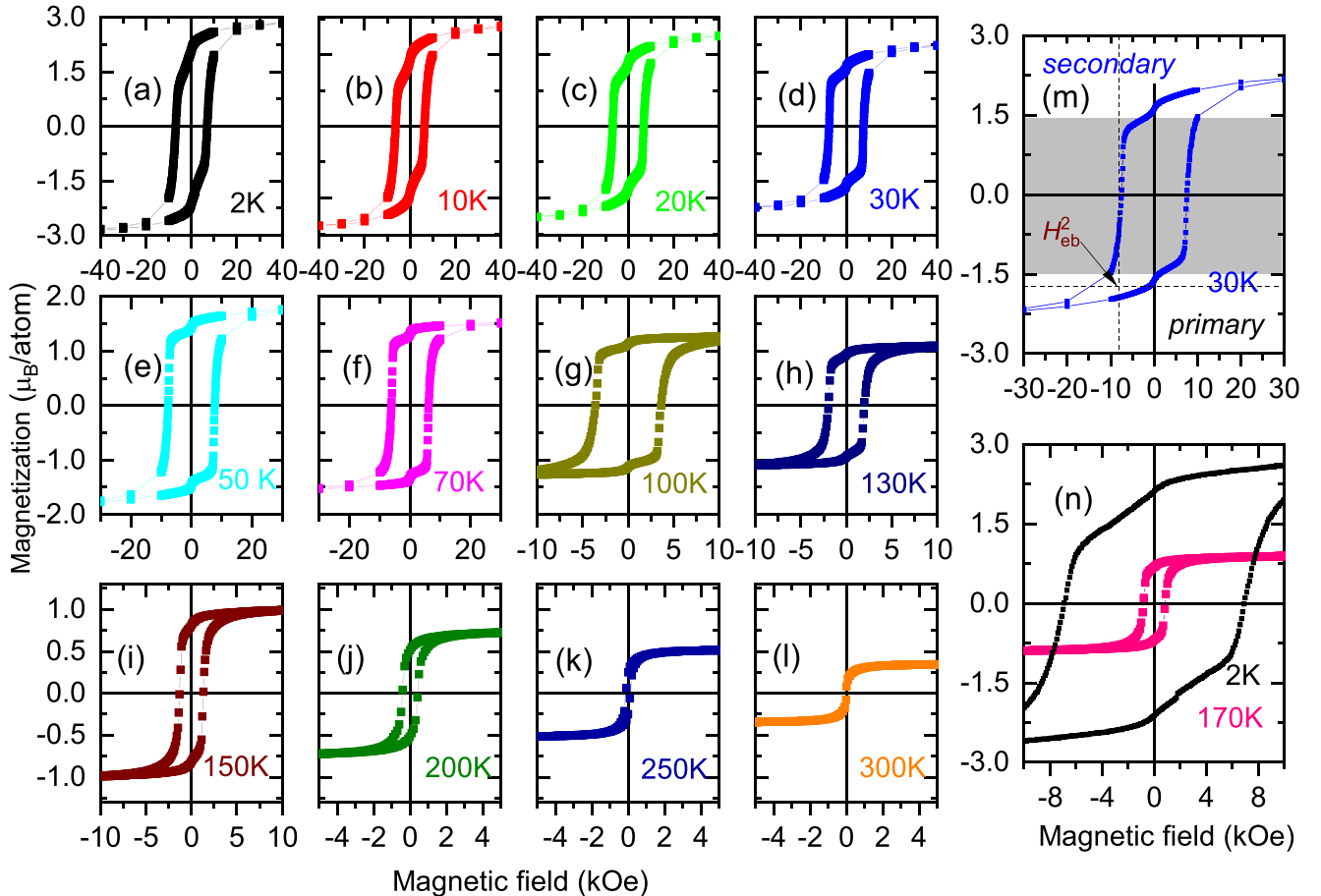


FIG. 10. Hysteresis loops for S3. (a)–(l) Hysteresis loops at various temperatures with temperature after field-cooling. (m), (n) Zoomed-in plots of the DHL loop shifts rendering $H_{cb}^{-/+}$ values at 30 K, and 2 K, 170 K. The shaded region in gray indicates the region of the primary loop. The H_{cb}^2 value is indicated by arrows in the bottom half of the loops at 30 K.

separates a nonergodic (SSG) phase from an ergodic (SPM) one. The plots of $H_a^{2/3}$ as a function of T_{irr} are shown in Fig. 17(b). The fitted lines (red dashed) intersect the x axis at $T_{\text{irr}}(0) \approx 318$ K, indicating a collective freezing spin-glass type of behavior for S3 at zero field.

D. Exchange bias at the interfaces of Ho/Er and Ho/Tb multilayers

Table II enlists the different parameters extracted from the magnetization measurements. Interestingly, one may note that the exchange bias strengths are higher for [Er₂₁/Tb_{7,21}] [5,6] and [Ho₂₉/Tb_{7,21}] [7], reported earlier, as compared to [Ho_{7,29}/Er₂₁] in the present case.

From the H_c versus temperature curves of Ho/Er [Figs. 11(c) and 12(a)] and Ho/Tb multilayers [7] we find shifts in the two temperature regimes of magnetic behaviors related to the conical-to-helical ($T_{\text{F1}(0)}$) and helical-to-paramagnetic (Ho) or helical-to-paramagnetic (Er) phases ($T_{\text{F2}(0)}$), respectively. In Ho/Er multilayers, $T_{\text{F1}(0)}$ reduces by 15 K as ML_{Ho} increases from 7 to 29. In Ho/Tb multilayers, however, $T_{\text{F1}(0)}$ increases by 31 K as ML_{Tb} increases from 7 to 21. Therefore, these shifts indicate increased profoundness of the Tb spin-spiral affecting the Ho/Tb spin configurations as compared to that of the Ho spin-spiral affecting the Ho/Er

spin configurations. This effect on spin spiral can be due to the FM ordering in Tb as compared to the conical ordering in Ho. Moreover, we find no transition phase for the present Ho/Er system ($\Delta R = 0$ K), which was reported earlier for the Ho/Tb system ($\Delta R \approx 42$ K [7]), or in Er/Tb system ($\Delta R \approx 22$ K [6]) when $ML_{\text{Tb}} = 21$. Thus, the existence of ΔR in Ho/Tb multilayers can be again due to the Tb moments affecting the Ho spin configurations below the temperature where Tb is expected to be in its FM phase. Furthermore, no significant temperature variation of the characteristic ZFC peaks due to the effect of applied fields is seen, which confirms their magnetic rigidity.

The lower bias fields in Table II for the Ho/Er multilayers as compared to Ho/Tb multilayers can be attributed to the weak coupling between the number of spin imbalances in Ho and Er. One may note that in both Ho and Er there exist stabilized conical structures. However, the cone angle between the c axis and the moments is larger in Ho, which is about 80° at 4 K as compared to Er where it is about 30° in Er [15]. Also, while the moments are confined to the a -plane for Er in the helical temperature range, the turn angle between the moments in successive planes of Ho averages 30° in the temperature range of the helix. Thus, the angle that each magnetic sublattice plane subtends with the next is higher in Ho, which can contribute more to the sublattice disorder

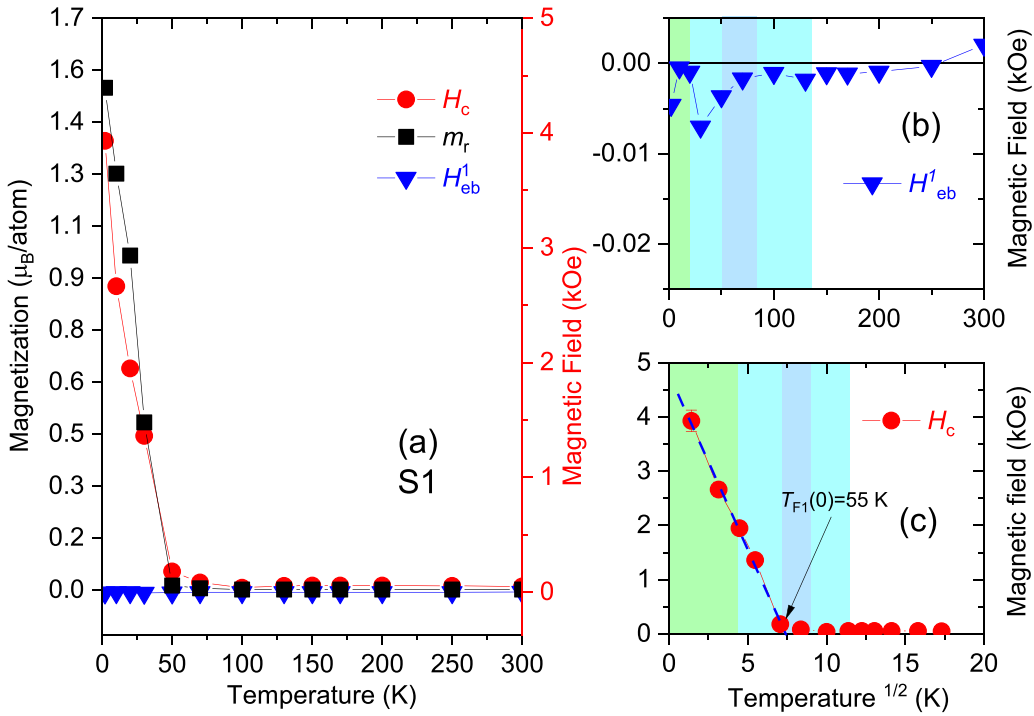


FIG. 11. H_c , H_{eb} , and m_r for S1. (a) Remanent magnetization m_r , coercive field H_c , and exchange bias field H_{eb}^1 as a function of temperature. (b) The zoomed-in plot of H_{eb}^1 vs temperature. (c) The H_c vs $T^{1/2}$ plot and its linear fit (blue dashed line) showing the maximum for the zero-field-cooled (ZFC) curves $T_{\text{F}1}(0)=55$ K. The shaded regions mark the temperature ranges of helical (cyan), conical (lime) phases for Ho, and sinusoidal (blue) phase of Er in bulk.

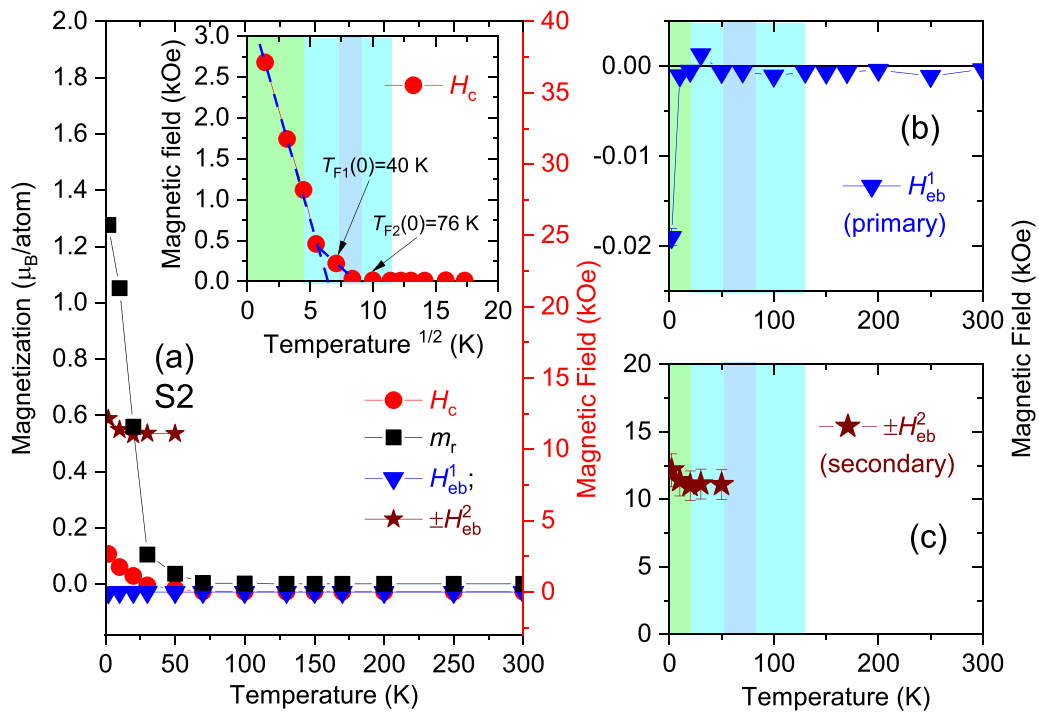


FIG. 12. H_c , H_{eb} , and m_r for S2. (a) Remanent magnetization m_r , coercive field H_c , and exchange bias field $H_{\text{eb}}^{1,2}$ as a function of temperature. The H_c vs $T^{1/2}$ plot and its linear fit (blue dashed line) showing the maximum for the zero-field-cooled (ZFC) curves $T_{\text{F}1}(0)=40$ K and $T_{\text{F}2}(0)=76$ K in the inset. (b) The zoomed-in plot of H_{eb}^1 vs temperature. (c) The plot of $\pm H_{\text{eb}}^2$ vs temperature. The shaded regions mark the temperature ranges of helical (cyan), conical (lime) phases for Ho, and sinusoidal (blue) phase of Er in bulk.

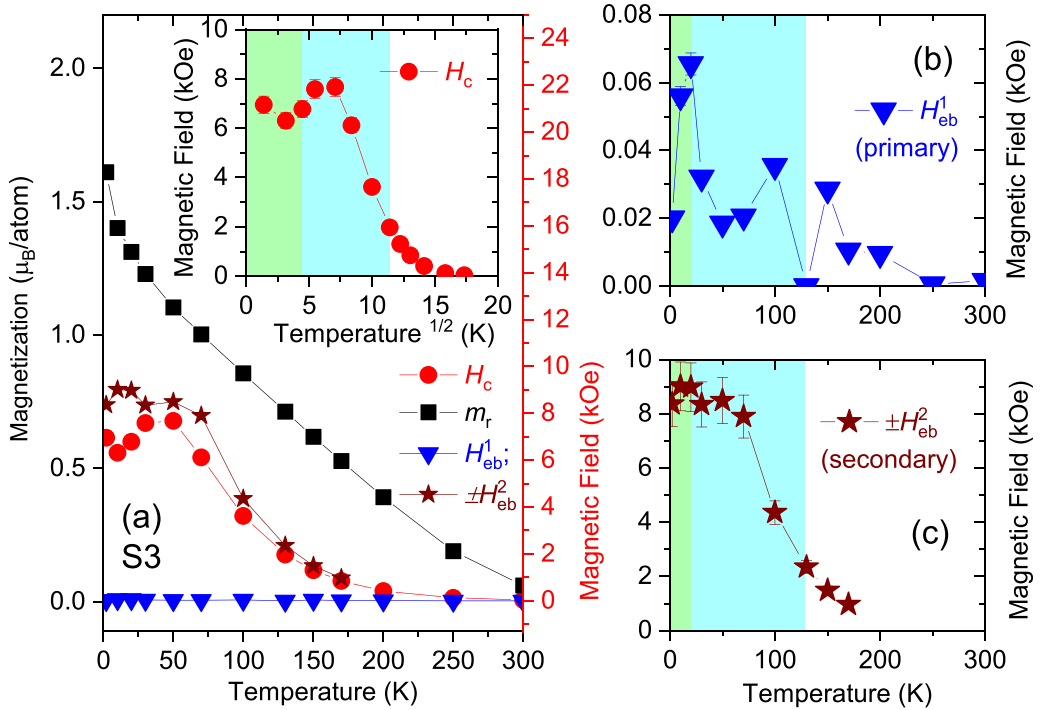


FIG. 13. H_c , H_{eb} , and m_r for S3. (a) Remanent magnetization m_r , coercive field H_c , and exchange bias field $H_{eb}^{1,2}$ as a function of temperature. The H_c vs $T^{1/2}$ plot is shown in the inset. (b), (c) The plots of H_{eb}^1 on a zoomed-in plot and $\pm H_{eb}^2$ vs temperature. The shaded regions mark the temperature ranges of helical (cyan) and conical (lime) phases for Ho in bulk.

during the field-cooling process as compared to in Er. This was the reason that we observed earlier higher exchange bias

fields for the Ho/Tb multilayers [7] as compared to that for the Er/Tb ones [6].

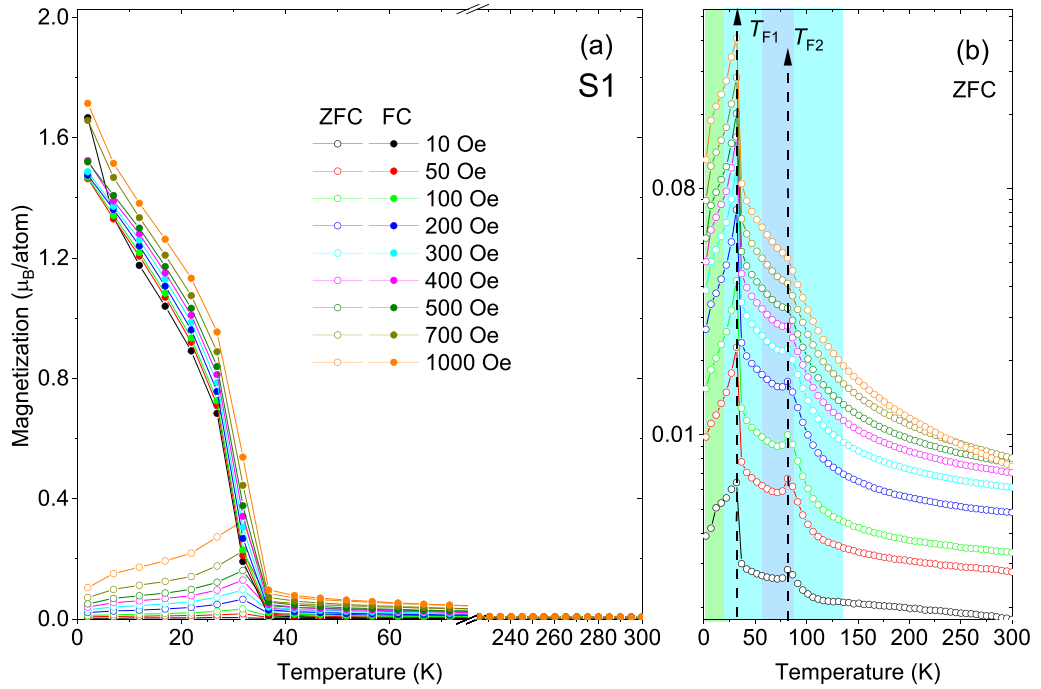


FIG. 14. FC-ZFC measurements for S1. (a) Temperature dependence of the dc magnetization. The measurements were done on heating at different fields after zero-field-cooling (ZFC) and field-cooling (FC) in 70 kOe (7000 mT). The inset shows a maximum (at lower temperatures) for the zoomed-in ZFC curves ($T_{F1,F2}$). The peak positions with increasing H_a are indicated by a dashed line, which shows no variation. The shaded regions mark the temperature ranges of helical (cyan), conical (lime) phases for Ho, and sinusoidal (blue) phase of Er in bulk.

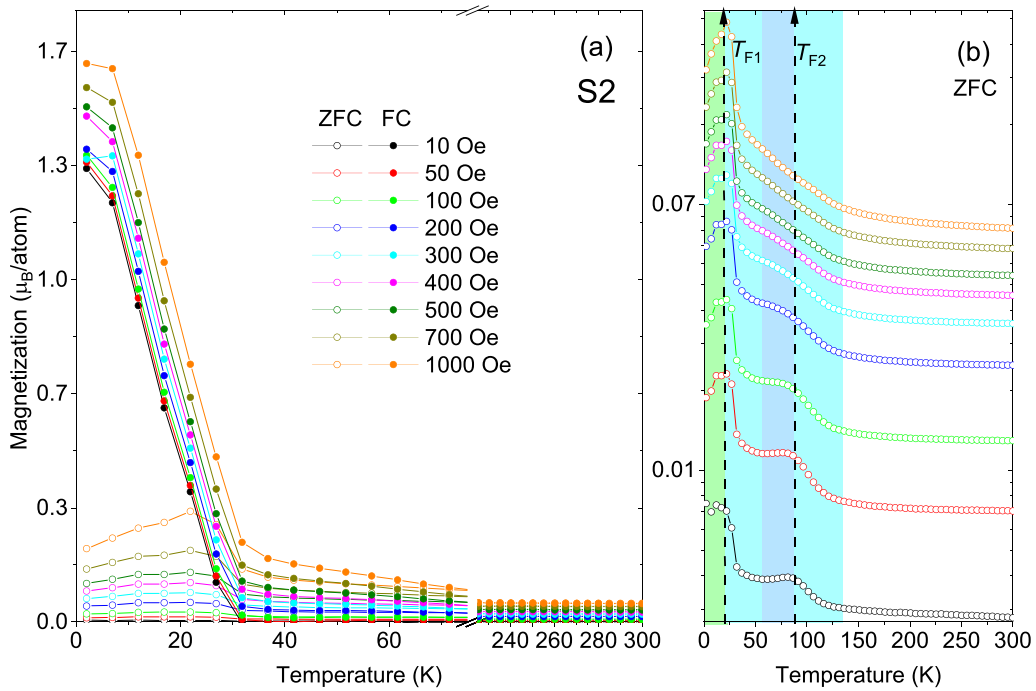


FIG. 15. FC-ZFC measurements for S2. (a) Temperature dependence of the dc magnetization. The measurements were done on heating at different fields after zero-field-cooling (ZFC) and field-cooling (FC) in 70 kOe (7000 mT). The inset shows a maximum (at lower temperatures) for the zoomed-in ZFC curves (T_{F1}, T_{F2}). The peak positions with increasing \mathbf{H}_a are indicated by the dashed lines, which show no variation. The shaded regions mark the temperature ranges of helical (cyan), conical (lime) phases for Ho, and sinusoidal (blue) phase of Er in bulk.

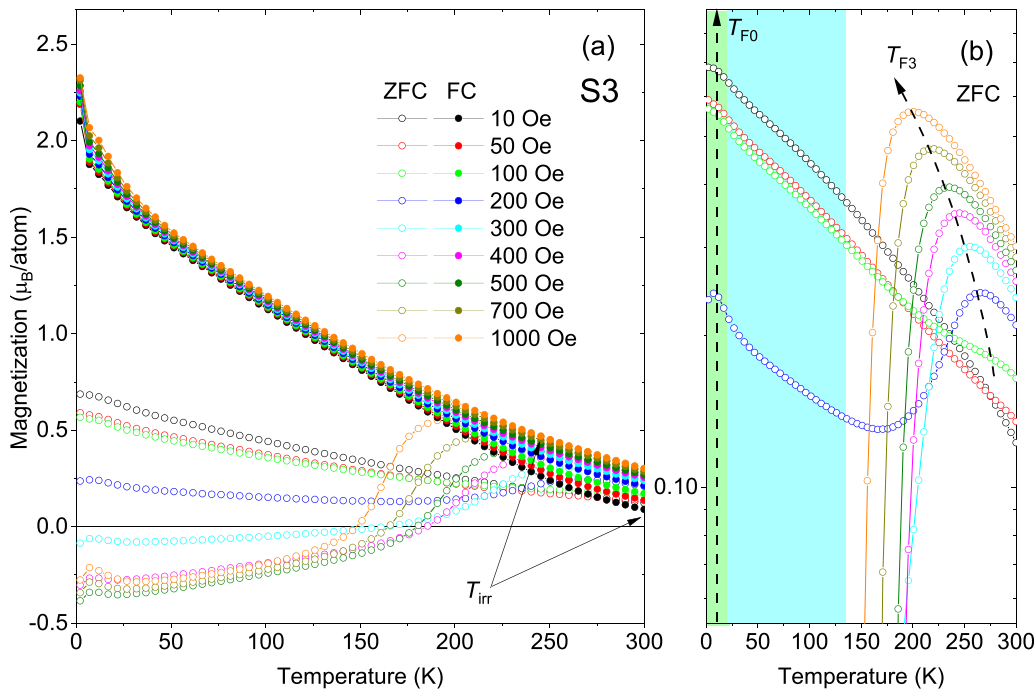


FIG. 16. FC-ZFC measurements for S3. (a) Temperature dependence of the dc magnetization. The measurements were done on heating at different fields after zero-field-cooling (ZFC) and field-cooling (FC) in 70 kOe (7000 mT). The T_{irr} are indicated by the arrows. (b) Two maxima for the zoomed-in ZFC curves (T_{F0}) at a lower temperature and (T_{F3}) at higher temperatures. The peak positions with increasing \mathbf{H}_a are indicated by the dashed lines, which show no variation for T_{F0} but varying T_{F3} . The shaded regions mark the temperature ranges of helical (cyan) and conical (lime) phases for Ho in bulk.

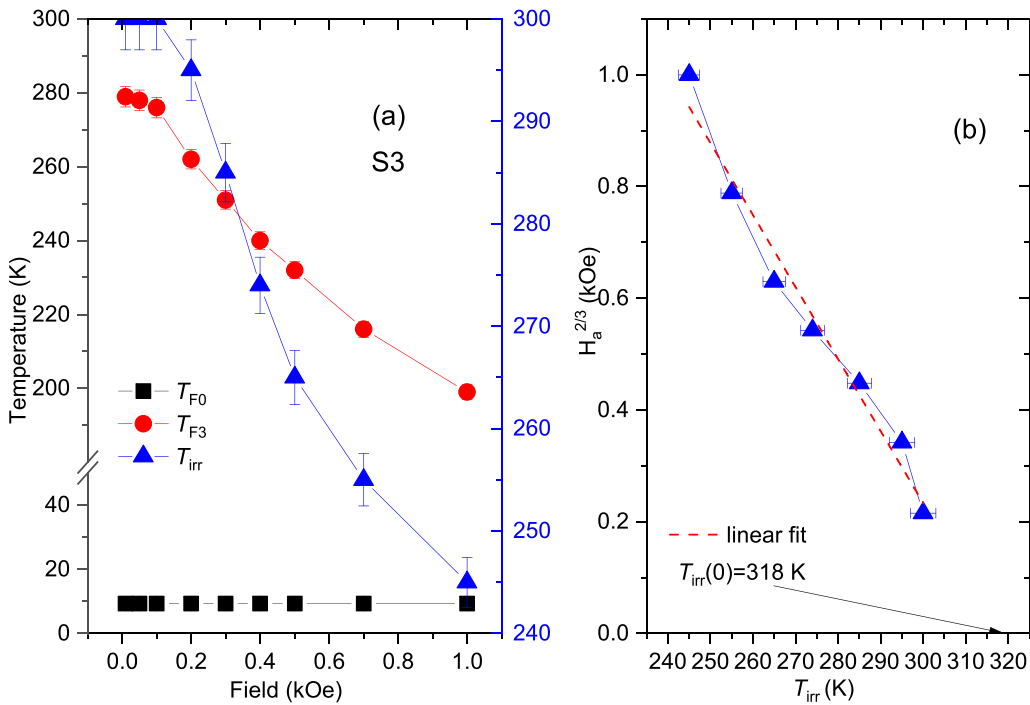


FIG. 17. Freezing and irreversible temperatures for S3. (a) T_{F0} and T_{F3} as estimated from the ZFC curves, and T_{irr} as estimated from the FC-ZFC curves plotted as a function of \mathbf{H}_a for S3. The lines are a guide to the eye. (b) The plot of $\mathbf{H}_a^{2/3}$ vs T_{irr} , which is fitted (red dashed line) following the Almeida-Thouless (AT) equation.

One may note that in the earlier cases [6,7], the coupling below 20 K was essentially between a RE (Tb) in its FM configuration and a RE (Ho or Er) in its conical phase. Thus, with an increase in ML_{Tb} from 7 or 5 to 21, we found an expected decrease of the bias fields for both systems. The decrease is basically due to the increase in the FM layer (here Tb is FM below 221 K) thickness. In the present case, as ML_{Ho} increases from 7 to 29, we find an increase in the bias

field (Table II). Note that for $ML_{Ho} = 29$, the turn angle is accumulated across ≈ 30 (3×10 MLs below 40 K) atomic layers, whereas for $ML_{Ho} = 7$, it is across ≈ 7 atomic layers only. The threefold increase in coupling in Ho/Er multilayers for $ML_{Ho} = 29$ is therefore due to the coupling between the spin-imbalance contributions ($J_{\Delta RE1}$, $J_{\Delta RE2}$) embedded within the $J_{\text{imbalance}}^{\text{inter}}$ terms, which increases with the thickness of the Ho layer, while the $J_{\text{imbalance}}^{\text{intra}}$ and inter- and intrasublattice

TABLE II. Parameters extracted from the magnetization measurements of RE/RE multilayers. The parameters from earlier reports are also included for comparison. The columns indicate the conical (marked in lime), helical (marked in cyan) phases in Ho (Er), while those marked in gray, indicate the range of helical phase in Tb.

Multilayer	d_{RE1}/d_{RE2} (nm)/(nm)	$T_{F1(0)}$ (K)	$T_{F2(0)}$ (K)	ΔR (K)	T_{F0} (K)	T_{F1} (K)	T_{F2} (K)	T_{F3} (K)	H_{eb}^1 (kOe)
[Dyx Tby] ₁₀ ; x,y = number of MLs									
[Dy ₁₈ Tb ₁₈] [4]	5.0/5.0	—	210	—	—	—	—	180–120	0.88 ± 0.01 (10 K)
[Dy ₃₆ Tb ₃₆] [4]	10.0/10.0	—	205	—	—	—	—	200–100	0.65 ± 0.01 (10 K)
[Erx Tby] ₁₀ ; x,y = number of MLs									
[Er ₂₁ Tb ₅] [5]	6.0/1.5	56	150	—	7	26	50	—	0.17 ± 0.01 (5 K)
[Er ₂₁ Tb ₂₁] [6]	6.0/6.0	72	196	22	—	35	100–150	200	0.013 ± 0.005 (2 K)
[Ho _x Tby] ₁₀ ; x,y = number of MLs									
[Ho ₂₉ Tb ₇] [7]	8.0/2.0	25	100	—	13	36	134	—	-0.57 ± 0.01 (2 K)
[Ho ₂₉ Tb ₂₁] [7]	8.0/6.0	56	205	42	—	35	127	—	-0.055 ± 0.005 (2 K)
[Ho _x Er _y] ₁₀ ; x,y = number of MLs									
[Ho ₇ Er ₂₁]: S1	2.0/6.0	55	—	—	—	33	82	—	-0.007 ± 0.001 (30 K)
[Ho ₂₉ Er ₂₁]: S2	8.0/6.0	40	76	—	—	20	89	—	-0.02 ± 0.005 (2 K)

terms are practically negligible. Thus, since there exists no possibility of coupling between the FM phase of an RE with the conical phase of another RE, as observed earlier [6,7], we find an overall decrease in the exchange bias fields for the Ho/Er system.

IV. SUMMARY AND CONCLUSION

We report here on the magnetic properties of Ho-Er interfaces of highly textured multilayers grown for two different Ho thicknesses ($ML_{Ho} = 7$ and 29) representing commensurable structures for fixed MLs of Er ($ML_{Er} = 21$). The different individual thicknesses are used to explore the effect of the fraction of the spin spiral of Ho and thereby the corresponding spin imbalances induced by sublattice disorder in the conical phase of Ho.

A meager exchange bias coupling (up to $H_{eb}^1 = -0.007 \pm 0.001$ kOe) in the range of the conical phase of Ho below 20 K was observed for $ML_{Ho} = 7$, which decreases significantly for higher temperatures as we go through the helical phase of Ho. Interestingly, a significant (threefold) increase in exchange bias of up to -0.02 ± 0.005 kOe is observed for $ML_{Ho} = 29$.

Analysis of the H_c versus temperature curves indicates two different magnetic behavior regimes ($\Delta r_{S1}^1 = 55$ K and $\Delta r_{S2}^1 = 33$ K; $\Delta r_{S1}^2 = 0$ K and $\Delta r_{S2}^2 = 43$ K). The first regime is related to the conical-to-helical phase and the second one to the helical-to-paramagnetic phase in Ho or helical-to-paramagnetic phase in Er. The first regime shifts to a lower temperature for an increased number of Ho MLs ($ML_{Ho} = 29$). Similarly, a decrease of 13 K is observed for the characteristic peak (T_{F1}) around the low-temperature

regime, which is around the temperature of the conical-to-helical phase of Ho or Er. However, no significant shift is noted for the high-temperature regime (T_{F2}), which is around that of the helical-to-paramagnetic phases of Ho. By replacing Er with CoFe in Ho/CoFe multilayers, we observe the usual DHLs and substantial exchange bias ($H_{eb}^1 = 0.07$ kOe ± 0.01 kOe; $H_{eb}^2 = 9.0 \pm 1$ kOe) as usually observed earlier for similar FM-RE systems such as Er/CoFe [6].

In conclusion, we find increased statistical spin imbalance in the number of magnetic sublattice disorders with Ho/Er multilayers due to an increase in the number of Ho MLs. The magnetic repeat distance being ten atomic layers below 40 K, $ML_{Ho} = 29$ can accumulate thrice as much magnetic periodicity as within $ML_{Ho} = 7$. Consequently, this leads to more irreversible moments in the RE, thereby contributing to an increase in the exchange bias by approximately threefold, relevant for the conical phase of Ho.

ACKNOWLEDGMENTS

We would like to thank the Electron Microscopy Center at the GTIIT for TEM measurements.

X.X., K.Z., and Y.C. did the sample preparation, magnetization, and the TEM measurements supervised by A.P. The data treatment for the magnetization measurements were done by X.X., K.Z., Y.C., C.Q., Z.W., and Y.Y. under the supervision of A.P. All authors reviewed the manuscript. A.P. conceived and designed the work, analyzed the data, coordinated the work, and wrote the manuscript.

The authors declare no competing interests.

-
- [1] A. Paul, S. Mukherjee, W. Kreuzpaintner, and P. Böni, Exchange-bias-like coupling in a ferrimagnetic multilayer Fe-Tb, *Phys. Rev. B* **89**, 144415 (2014).
 - [2] S. Mukherjee, W. Kreuzpaintner, J. Stahn, J.-G. Zheng, A. Bauer, P. Böni, and A. Paul, Exchange-bias-like coupling in a Cu-diluted-Fe-Tb multilayer, *Phys. Rev. B* **91**, 104419 (2015).
 - [3] S. Fust, S. Mukherjee, N. Paul, J. Stahn, W. Kreuzpaintner, P. Böni, and A. Paul, Realizing topological stability of magnetic helices in exchange coupled multilayers for all-spin-based system, *Sci. Rep.* **6**, 33986 (2016).
 - [4] J. Ye, T. Baldauf, S. Mattauch, N. Paul, and A. Paul, Topologically stable helices in exchange coupled rare-earth/rare-earth multilayer with superspin-glass like ordering, *Commun. Phys.* **2**, 114 (2019).
 - [5] J. Huang, C. Liu, B. Yuan, X. Xiao, and A. Paul, Exchange coupling due to spin-imbalance in Er magnetic sublattice within Er/Tb multilayers, *J. Magn. Magn. Mater.* **585**, 171108 (2023).
 - [6] X. Xiao, K. Zhao, Y. Cui, J. Chen, J. Liao, B. Du, and A. Paul, Exchange coupling at the interfaces of Er-Tb and Er-CoFe multilayers, *J. Phys. Chem. C* **127**, 20549 (2023).
 - [7] X. Xiao, K. Zhao, Y. Cui, H. Liu, Y. Wei, S. Yang, and A. Paul, Exchange coupling in the conical phase of Ho within Ho/Tb multilayers due to Ho magnetic sublattice disorder, *Phys. Rev. B* **109**, 174422 (2024).
 - [8] S. Jenkins, W. J. Fan, R. Gaina, R. W. Chantrell, T. Klemmer, and R. F. L. Evans, The atomistic origin of exchange anisotropy in non-collinear IrMn/CoFe, *Phys. Rev. B* **102**, 140404(R) (2020).
 - [9] R. Skomski, Finite-temperature behavior of anisotropic two-sublattice magnets, *J. Appl. Phys.* **83**, 6724 (1998).
 - [10] J. J. Rhyne and A. E. Clark, Magnetic anisotropy of terbium and dysprosium, *J. Appl. Phys.* **38**, 1379 (1967).
 - [11] P. De. V. Du Plessis, Magnetic anisotropy of some heavy rare-earth metals, *Physica* **41**, 379 (1969).
 - [12] Yu. S. Vishnyakov, V. L. Ivannikov, R. Z. Levitin, and B. K. Ponomarev, Determination of the magnetic uniaxial anisotropy constants of holmium from magnetization measurements in fields up to 240 kOe, *Zh. Eksp. Teor. Fiz.* **57**, 1956 (1969) [*Sov. Phys. JETP* **30**, 1059 (1970)].
 - [13] R. J. Radwanski, The origin of the basal-plane magnetocrystalline anisotropy in 4f Co-rich intermetallics, *J. Phys. F: Met. Phys.* **17**, 267 (1987).
 - [14] *Advanced Magnetism and Magnetic Materials, Aspects of Rare Earth - Transition Metal Intermetallics*, edited by N. H. Duc (Vietnam National University Press, Hanoi, 2014), Vol. 1.
 - [15] J. Jensen and A. R. Mackintosh, *Rare Earth Magnetism: Structures and Excitations* (Clarendon Press, Oxford, 1991).
 - [16] T. Kosugi, S. Kawano, N. Achiwa, A. Onodera, Y. Nakai, and N. Yamamoto, Direct evidence of helian structures in holmium by single crystal neutron diffraction, *Physica B* **334**, 365 (2003).

- [17] J. D. S. Witt, J. F. K. Cooper, N. Satchell, C. J. Kinane, P. J. Curran, S. J. Bending, S. Langridge, L. J. Heyderman, and G. Burnell, Magnetic phases of sputter deposited thin-film erbium, *Sci. Rep.* **6**, 39021 (2016).
- [18] J. W. Cable, E. O. Wollan, W. C. Koehler, and M. K. Wilkinson, Magnetic structures of metallic erbium, *Phys. Rev.* **140**, A1896 (1965).
- [19] R. A. Cowley and J. Jensen, Magnetic structures and interactions in erbium, *J. Phys.: Condens. Matter* **4**, 9673 (1992).
- [20] J. Jensen, Molecular field calculation of the magnetic structure in erbium, *J. Phys. F* **6**, 1145 (1976).
- [21] J. A. Borchers, M. B. Salamon, R. W. Erwin, J. J. Rhyne, R. R. Du, and C. P. Flynn, Structural and magnetic properties of Er thin films and Er/Y superlattices: Magnetoelastic effects, *Phys. Rev. B* **43**, 3123 (1991).
- [22] J. Kwo, M. Hong, and S. Nakahara, Growth of rare-earth single crystals by molecular beam epitaxy: The epitaxial relationship between hcp rare earth and bcc niobium, *Appl. Phys. Lett.* **49**, 319 (1986).
- [23] J. Yu, Exploring the magnetic phases in dysprosium by neutron scattering techniques, Ph.D. thesis, University of Alabama, 2014.
- [24] A. R. Wildes, J. Mayer, and K. Theis-Bröhl, The growth and structure of epitaxial niobium on sapphire, *Thin Solid Films* **401**, 7 (2001).
- [25] A. Paul, T. Damm, D. E. Bürgler, S. Stein, H. Kohlstedt, and P. Grünberg, Correlation of magnetotransport and structure in sputtered Co/Cu multilayers, *J. Phys.: Condens. Matter* **15**, 2471 (2003).
- [26] M. Kiwi, J. Mejía-López, R. D. Portugal, and R. Ramírez, Positive exchange bias model: Fe/FeF₂ and Fe/MnF₂ bilayers, *Solid State Commun.* **116**, 315 (2000).
- [27] A. Paul, N. Paul, P. Müller-Buschbaum, A. Bauer, and P. Böni, Superparamagnetic regular nanopillar-like structures studied by grazing-incidence x-ray scattering: Effect of vertical correlation, *J. Appl. Cryst.* **47**, 1065 (2014).
- [28] M. Knobel, W. C. Nunes, L. M. Socolovsky, E. D. Biasi, J. M. Vargas, and J. C. Denardin, Superparamagnetism and other magnetic features in granular materials: A review on ideal and real systems, *J. Nanosci. Nanotechnol.* **8**, 2836 (2008).
- [29] J. A. Mydosh, Spin glasses: Redux: an updated experimental/materials survey, *Rep. Prog. Phys.* **78**, 052501 (2015).
- [30] J. R. L. de Almeida and D. J. Thouless, Stability of the Sherrington-Kirkpatrick solution of a spin glass model, *J. Phys. A: Math. Gen.* **11**, 983 (1978).